

# 1 On the drivers of droplet variability in Alpine mixed-phase 2 clouds

3  
4 Paraskevi Georgakaki<sup>1</sup>, Aikaterini Bougiatioti<sup>2</sup>, Jörg Wieder<sup>3</sup>, Claudia Mignani<sup>4</sup>, Fabiola  
5 Ramelli<sup>3</sup>, Zamin A. Kanji<sup>3</sup>, Jan Henneberger<sup>3</sup>, Maxime Hervo<sup>5</sup>, Alexis Berne<sup>6</sup>, Ulrike  
6 Lohmann<sup>3</sup> and Athanasios Nenes<sup>1,7</sup>

7 <sup>1</sup>Laboratory of Atmospheric Processes and their Impacts, School of Architecture, Civil & Environmental  
8 Engineering, École Polytechnique Fédérale de Lausanne, Lausanne, CH-1015, Switzerland

9 <sup>2</sup>Institute for Environmental Research & Sustainable Development, National Observatory of Athens, P. Penteli,  
10 GR-15236, Greece

11 <sup>3</sup>Department of Environmental Systems Science, Institute for Atmospheric and Climate Science, ETH Zurich,  
12 Zurich, CH-8092, Switzerland

13 <sup>4</sup>Department of Environmental Sciences, University of Basel, Basel, CH-4056, Switzerland

14 <sup>5</sup>Federal Office of Meteorology and Climatology, MeteoSwiss, Payerne, CH-1530, Switzerland

15 <sup>6</sup>Environmental Remote Sensing Laboratory, School of Architecture, Civil & Environmental Engineering, École  
16 Polytechnique Fédérale de Lausanne, Lausanne, CH-1015, Switzerland

17 <sup>7</sup>Center for Studies of Air Quality and Climate Change, Institute of Chemical Engineering Sciences, Foundation  
18 for Research and Technology Hellas, Patras, GR-26504, Greece

19 *Correspondence to:* Athanasios Nenes ([athanasios.nenes@epfl.ch](mailto:athanasios.nenes@epfl.ch)).  
20

## 21 Abstract

22 Droplet formation provides a direct microphysical link between aerosols and clouds (liquid or  
23 mixed phase), and its adequate description poses a major challenge for any atmospheric model.  
24 Observations are critical for evaluating and constraining the process. Towards this, aerosol size  
25 distributions, cloud condensation nuclei, hygroscopicity and lidar-derived vertical velocities  
26 were observed in Alpine mixed-phase clouds during the Role of Aerosols and Clouds Enhanced  
27 by Topography on Snow (RACLETS) field campaign in the Davos, Switzerland region during  
28 February and March 2019. Data from the mountain-top site of Weissfluhjoch (WFJ) and the  
29 valley site of Davos Wolfgang are studied. These observations are coupled with a state-of-the  
30 art droplet activation parameterization to investigate the aerosol-cloud droplet link in mixed-  
31 phase clouds. The mean CCN-derived hygroscopicity parameter,  $\kappa$ , at WFJ ranges between  
32 0.2-0.3, consistent with expectations for continental aerosol.  $\kappa$  tends to decrease with size,  
33 possibly from an enrichment in organic material associated with the vertical transport of fresh  
34 ultrafine particle emissions (likely from biomass burning) from the valley floor in Davos. The  
35 parameterization provides droplet number that agrees with observations to within ~25%. We  
36 also find that the susceptibility of droplet formation to aerosol concentration and vertical  
37 velocity variations can be appropriately described as a function of the standard deviation of the  
38 distribution of updraft velocities,  $\sigma_w$ , as the droplet number never exceeds a characteristic limit,  
39 termed “limiting droplet number”, of  $\sim 150\text{-}550\text{ cm}^{-3}$ , which depends solely on  $\sigma_w$ . We also  
40 show that high aerosol levels in the valley, most likely from anthropogenic activities, increase

41 cloud droplet number, reduce cloud supersaturation ( $<0.1\%$ ) and shift the clouds to a state that  
42 is less susceptible to aerosol and become very sensitive to vertical velocity variations. The  
43 transition from aerosol to velocity-limited regime depends on the ratio of cloud droplet number  
44 to the limiting droplet number, as droplet formation becomes velocity-limited when this ratio  
45 exceeds 0.565. Under such conditions, droplet size tends to be minimal, reducing the likelihood  
46 that large drops are present that would otherwise promote glaciation through rime splintering  
47 and droplet shattering. Identifying regimes where droplet number variability is dominated by  
48 dynamical – rather than aerosol – changes is key for interpreting and constraining when and  
49 which types of aerosol effects on clouds are active.

50

## 51 **1. Introduction**

52 Orographic clouds, and the precipitation they generate, play a major role in Alpine weather and  
53 climate (e.g., Roe, 2005; Grubisic and Billings, 2008; Saleeby et al., 2013; Vosper et al., 2013;  
54 Lloyd et al., 2015). The formation and evolution of orographic clouds involves a rich set of  
55 interactions at different spatial and temporal scales encompassing fluid dynamics, cloud  
56 microphysics and orography (Roe, 2005; Rotunno and Houze, 2007). Atmospheric aerosol  
57 particles modulate the microphysical characteristics of orographic clouds by serving as cloud  
58 condensation nuclei (CCN) that form droplets, or ice nucleating particles (INPs) that form ice  
59 crystals (e.g., Pruppacher and Klett, 1997; Muhlbauer and Lohmann, 2009; Zubler et al., 2011;  
60 Saleeby et al., 2013).

61 Emissions of aerosol particles acting as CCN and INPs can affect the microphysical and  
62 radiative properties of clouds with strong (but highly uncertain) effects on local and regional  
63 climate (IPCC, 2013; Seinfeld et al., 2016). Aerosol interactions with orographic clouds are  
64 subject to even larger uncertainties, owing in part to the complex flows generated by the  
65 interaction of the large-scale flow with the mesoscale orographic lifting and condensation, and  
66 complex anisotropic turbulent air motions that arise (Roe, 2005; Smith, 2006; Rotunno and  
67 Houze, 2007). Most importantly, orographic clouds are often mixed-phase clouds (MPCs),  
68 which are characterized by the simultaneous presence of supercooled liquid water droplets and  
69 ice crystals (Lloyd et al., 2015; Farrington et al., 2016; Lohmann et al., 2016; Henneberg et al.,  
70 2017). MPCs remain one of the least understood cloud types, due to the multiple and highly  
71 nonlinear cloud microphysical pathways that can affect their properties and evolution. MPCs  
72 tend to glaciate (i.e., transition to pure ice clouds) over time because of the Bergeron-Findeisen  
73 process, which is the rapid growth of ice crystals at the expense of the evaporating cloud

74 droplets, owing to the higher saturation vapor pressure of liquid water over ice (~~Bergeron,~~  
75 ~~1935; Findeisen, 1938~~~~Bergeron, 1935; Findeisen, 1938~~). Aerosol concentrations may also alter  
76 the microphysical pathways active in MPCs and ultimately drive their glaciation state. For  
77 instance, increase in CCN concentrations leads to more numerous and smaller cloud droplets,  
78 reducing the riming efficiency of ice crystals and therefore the hydrometeor crystal mass and  
79 the amount of precipitation (Lohmann and Feichter, 2005; Lance et al., 2011; Lohmann, 2017).  
80 This mechanism counters the glaciation indirect effect, where increases in INP concentrations  
81 elevate ice crystal number concentration (ICNC) and promotes the conversion of liquid water  
82 to ice - therefore the amount of ice-phase precipitation (Lohmann, 2002). Increases in CCN  
83 can also decrease cloud droplet radius, and impede cloud glaciation, owing to reductions in  
84 secondary ice production (SIP), which includes rime splintering, collisional break-up and  
85 droplet shattering (Field et al., 2017; Sotiropoulou et al., ~~2020a, 2020b~~2020, 2021).

86 Cloud-scale updraft velocity (i.e., the part of the vertical velocity spectrum with positive  
87 values) is the major driver of droplet formation, owing to the supersaturation generated from  
88 adiabatic expansion and cooling (e.g., Nenes et al., 2001; Ghan et al., 2011). Despite its  
89 importance, the simulation of updraft velocity by atmospheric models is rarely constrained by  
90 observations, which can lead to large uncertainties in climate and numerical weather prediction  
91 models (Sullivan et al., 2016, 2018). Reutter et al. (2009) pointed out that droplet formation in  
92 clouds can be limited by the amount of CCN present (called the “aerosol-limited” regime), or  
93 the vertical velocity that generates supersaturation in the cloudy updrafts (called the “velocity-  
94 limited” regime). Over the complex Alpine terrain, vertical motions can be significantly shaped  
95 by the effects of orography (Lohmann et al., 2016). Orographic MPCs have been frequently  
96 observed in the Swiss Alps under high updraft velocity conditions, where supersaturation with  
97 respect to liquid water is formed faster than it is depleted by diffusional and collisional ice  
98 growth processes (Korolev and Isaac, 2003) leading to persistent MPCs (Lohmann et al., 2016).

99 Given the importance of droplet number for the radiative cloud properties and  
100 microphysical evolution of Alpine MPCs, it is essential to understand the main aerosol and  
101 dynamics properties that drive droplet formation. A limited number of studies exist that discuss  
102 this very important topic, focusing though on liquid-phase clouds (Hammer et al., 2014, 2015;  
103 Hoyle et al., 2016). Hoyle et al. (2016) ~~demonstrated~~~~showed~~ that 79% of the variance in droplet  
104 number ~~observed~~ in warm ~~tropospheric~~ clouds formed ~~over~~at the high-altitude ~~research station~~  
105 ~~of Swiss Alps~~ Jungfrauoch ~~station~~ (3450 m a.s.l.) ~~in the Swiss Alps can be explained~~is driven  
106 by ~~the variations in~~ potential CCN ~~number concentrations~~~~concentration~~ (i.e. aerosol particles  
107 with a dry diameter >80 nm). With box model simulations, Hammer et al. (2015) investigated

108 the influence of updraft velocity, particle concentration and hygroscopicity on droplet  
109 formation ~~in cloud updraft~~, and found that variations in vertical wind velocity have the  
110 strongest influence on the aerosol activation. The ability to predict droplet number in MPCs,  
111 where the existence of ice crystals can deplete supersaturation or the low temperatures may  
112 decrease CCN activity through the formation of glassy aerosol, has not been assessed in a  
113 closure study to date.

114 Here we analyze observational data collected as part of the Role of Aerosols and Clouds  
115 Enhanced by Topography on Snow (RACLETS) field campaign, which was held in the region  
116 of Davos, Switzerland, during February and March 2019. This intensive field campaign aims  
117 to address questions related to the modulators of orographic precipitation, the drivers of the  
118 enhanced ice-crystal number concentrations observed in MPCs as well as the human-caused  
119 pollution effects on cloud microphysical and optical properties. Through this study we focus  
120 on a two-week period seeking to unravel the complex aerosol-droplet-updraft velocity  
121 interactions that occur in the orographic MPCs. For this, we combine CCN number  
122 concentrations with the particle size distributions to understand the variations in hygroscopicity  
123 over time and for sites located in the valley and a close by mountain-top site. The in-situ  
124 measurements are subsequently coupled with a state-of-the art droplet parameterization to  
125 determine the potential droplet numbers and the corresponding maximum supersaturation  
126 achieved in cloudy updrafts. The predicted droplet numbers are evaluated against direct  
127 observations, and the degree to which droplet formation is velocity- or aerosol-limited is  
128 determined for the whole timeseries.

129

## 130 **2. Methods**

### 131 2.1 Observational datasets

132 The analysis utilizes measurements collected during the RACLETS campaign, which took  
133 place from 8 February to 28 March 2019 ([https://www.envidat.ch/group/about/raclets-field-](https://www.envidat.ch/group/about/raclets-field-campaign)  
134 [campaign](https://www.envidat.ch/group/about/raclets-field-campaign)) (Mignani et al., 2020; Ramelli et al., 2020b, c; Lauber et al., 2020). This joint  
135 research project offers a unique dataset of orographic clouds, precipitation and snow  
136 measurements in an effort to shed light on some fundamental microphysical processes being  
137 present in subsequent stages of the lifecycle of clouds (i.e. cloud formation, precipitation onset,  
138 cloud dissipation). All measurements presented in this paper were performed at two distinct  
139 observation stations near Davos, Switzerland (supplement Fig. S1). A measurement site is  
140 located at Davos Wolfgang, which is the pass between Davos (1560 m a.s.l.) in the South and

141 Klosters (1200 m a.s.l.) in the North and is otherwise known as Wolfgang-Pass (WOP; 1630  
142 m a.s.l., 46°50'08.076"N 9°51'12.939"E). Measurements were also conducted at the mountain-  
143 top station Weissfluhjoch (WFJ; 2700 m a.s.l., 46°49'58.670"N 9°48'23.309"E), which is  
144 located ~1 km above the valley floor in Davos, in the eastern part of the Swiss Alps. The  
145 current study primarily focuses on data collected during a two-week period of interest, which  
146 spans from 24 February to 8 March 2019. During the RACLETS campaign, a defective sheath  
147 air filter affected the CCN measurements collected at WFJ, thus inhibiting data usage from the  
148 instrument for a large duration of the campaign. Therefore, we limit our analysis to the above-  
149 mentioned period, when the CCN counter was fully operational. Besides, during the selected  
150 period two distinct weather patterns were observed (fair weather conditions interrupted by a  
151 precipitating period), allowing for a contrasting analysis of the observed scenarios. The  
152 following description refers to the measurements that provided the basis for the present analysis  
153 (see Table 1).

154

#### 155 *2.1.1 Aerosol particle size distribution measurements*

156 Particle size distributions were continuously monitored at WOP and WFJ using commercially  
157 available Scanning Mobility Particle Sizers (SMPS; Model 3938, TSI Inc., US). At both  
158 stations, the systems consisted of a differential mobility analyzer (Model 3081, TSI Inc., US),  
159 a soft X-ray neutralizer (Model 3088, TSI Inc., US) and a water-based condensation particle  
160 counter (Model 3787 at WOP, Model 3788 at WFJ, TSI Inc. US). Running the particle counters  
161 in low flow mode ( $0.6 \text{ Lmin}^{-1}$ ), using a sheath flow of  $5.4 \text{ Lmin}^{-1}$  and applying a total scanning  
162 time of 2 minutes (scan time: 97 s, retrace time: 3 s, purge time: 10 s), particle size distributions  
163 between 11.5 nm and 469.8 nm diameter were monitored.

164

#### 165 *2.1.2 CCN measurements*

166 A Droplet Measurement Technologies (DMT) single-column continuous-flow streamwise  
167 thermal gradient chamber (CFSTGC; Roberts and Nenes, 2005) was used to carry out in-situ  
168 measurements of CCN number concentrations for different supersaturations ( $SS$ ). The  
169 CFSTGC consists of a cylindrical flow tube with wetted walls, inside which  $SS$  is developed  
170 by applying a linear streamwise temperature gradient between the column top and bottom.  
171 Owing to the greater mass diffusivity of water vapor than the thermal diffusivity of air, a  
172 constant and controlled  $SS$  is generated with a maximum at the centerline of the flow tube. The  
173  $SS$  is mainly dependent on the applied temperature gradient, flow rate and pressure (Roberts  
174 and Nenes, 2005). An aerosol sample flow is introduced at the column centerline, and those

175 particles having a critical supersaturation lower than the instrument *SS* will activate to form  
176 droplets and will afterward be counted and sized by an Optical Particle Counter (OPC) located  
177 at the base of the CFSTGC column. The *SS* developed within the instrument responds linearly  
178 to changes in pressure, since its operation relies on the difference between heat and mass  
179 diffusivity. Calibration of the instrument, which determines the output supersaturation, was  
180 performed by the manufacturer at ~800 mbar, while throughout the campaign the CFSTGC  
181 was operating at a lower pressure ~735 mbar, therefore the *SS* reported by the instrument is  
182 adjusted by a factor of  $\frac{735}{800} = 0.92$ , which ~~takes into account~~accounts for the difference  
183 between the ambient and the calibration pressure (Roberts and Nenes, 2005). CCN  
184 concentrations were measured at a specific *SS* for approximately 10 minutes; the instrument  
185 was cycled between 6 discrete values ranging from 0.09% to 0.74% supersaturations,  
186 producing a full spectrum every hour. Each 10-minute segment of the raw CCN data are filtered  
187 to discount periods of transient operation (during supersaturation changes), and whenever the  
188 room temperature housing the instrument changed sufficiently to induce a reset in column  
189 temperature (the instrument control software always sets the column temperature to be at least  
190 1.5 degrees above the room temperature to exclude spurious supersaturation generation in the  
191 column inlet). The CFSTGC was deployed on the mountain-top site of WFJ with the intention  
192 of relating the CCN measurements directly to the size distribution and total aerosol  
193 concentration data measured by the SMPS instrument at the same station.

194

### 195 2.1.3 Cloud microphysical measurements

196 In-situ observations of the cloud microphysical properties were obtained with the tethered  
197 balloon system HoloBalloon (Ramelli et al., 2020a). The main component of the measurement  
198 platform is the holographic cloud imager HOLIMO 3B, which uses digital in-line holography  
199 to image an ensemble of cloud particles in the size range from 6  $\mu\text{m}$  to 2 mm diameter in a  
200 three-dimensional detection volume. Note that particles smaller than 6  $\mu\text{m}$  are not detected by  
201 HOLIMO, which means that the droplet number concentration may be underestimated. Based  
202 on a set of two-dimensional images, information about the particle position, size and shape can  
203 be obtained. The detected particles can be classified as cloud droplets and ice crystals using  
204 supervised machine learning (Fugal et al., 2009; Touloupas et al., 2020). The differentiation  
205 between cloud droplets (circular) and ice crystals (non-circular) is possible~~done~~ for particles  
206 larger than~~exceeding~~ 25  $\mu\text{m}$  diameter based on their shape (Henneberger et al., 2013). From  
207 the classification, the phase-resolved size distribution, concentration and content can be derived

Formatted: English (United States)

(Henneberger et al., 2013; Ramelli et al., 2020a). ~~HOLIMO has an open-path configuration (i.e. the detection volume lies between the two instrument towers) and thus is also able to measure raindrops up to a size of  $\sim 2$  mm.~~ The HoloBalloon platform was flying at WOP and provided vertical profiles of the cloud properties within the lowest 300 meters of the boundary layer (BL). The current analysis utilizes the cloud droplet number concentration and liquid water content (LWC) measurements. Note that the LWC is calculated based on the ~~measured number concentration and~~ size distribution of the cloud droplets using a liquid water density ( $\rho_w$ ) of  $1000 \text{ kg m}^{-3}$  and is therefore dominated by large cloud particles.

**Table 1.** Overview of data sources from the RACLETS campaign used for this study. Along with the observed parameters, the corresponding instrumentation, measurements range and time resolutions are listed.

Measured parameter	Measurement site	Instrument	Measurement range	Time resolution
Aerosol number size distribution	WOP/ WFJ	Scanning Mobility Particle Sizer	11.5 – 469.8 nm	2 min
CCN number concentration	WFJ	Continuous flow streamwise thermal gradient CCN counter	SS = 0.09 – 0.74%	1 s
Cloud droplet number concentration and liquid water content	WOP	Holographic cloud imager HOLIMO	6 $\mu\text{m}$ – 2 mm	10 – 20 s
Precipitation	WOP/ WFJ	Parsivel disdrometer/ MeteoSwiss weather station	0.2 mm – 25 mm	30 s
Horizontal wind speed and direction	WOP/ WFJ	MeteoSwiss weather station	–	10-min averages
Profiles of vertical wind speed	WOP	Wind Doppler Lidar	200 m – 8100 m AGL	<del>up to</del> 5 s <u>max</u>

220

221 2.1.4 Meteorological data

222 During the measurement period, meteorological parameters (e.g., pressure, temperature,  
223 precipitation, horizontal wind speed and direction) were continuously monitored by the  
224 permanent MeteoSwiss observation station at WFJ. Additionally, a weather station was  
225 installed on the OceaNet container (Griesche et al., 2019) deployed at WOP, which also hosted  
226 several remote sensing instruments (e.g., Cloud radar, Raman Lidar, Microwave radiometer)  
227 and a Particle Size Velocity (Parsivel) disdrometer (Parsivel2, OTT HydroMet GmbH,  
228 Germany; Tokay et al., 2014) to measure precipitation. As there was no wind sensor included  
229 in the weather station on the OceaNet container, we utilized the horizontal wind speed and  
230 direction measurements from the nearby MeteoSwiss station in Davos, assuming that they  
231 provide a good proxy for the wind regime in the valley. Vertical wind speed profiles were  
232 obtained with a wind Doppler Lidar (WindCube 100S, manufactured by Leosphere) at WOP.  
233 Throughout the campaign the wind lidar measured from 200 m to 8100 m above ground level  
234 (AGL) with high temporal (~~up to~~ 5 s max) and vertical resolution (50 m). The wind lidar  
235 operated following the Doppler Beam Switching (~~DBS~~) technique with an elevation of 75°.  
236 More information about the remote sensing measurements can be found in Ramelli et al.  
237 (2020b).

238

239 2.2 Aerosol hygroscopicity

240 The aerosol hygroscopicity parameter,  $\kappa$ , encompasses the impact of particle chemical  
241 composition on its subsaturated water uptake and CCN activity (Petters and Kreidenweis,  
242 2007). Here, we determine  $\kappa$  similar to the approach of Moore et al. (2011), ~~Jurányi et al.~~  
243 ~~(2014)~~ [Jurányi et al. \(2011\)](#), Latham et al. (2013), Kalkavouras et al. (2019), Kacarab et al.  
244 (2020) and others, by combining the CCN measurements with the SMPS aerosol size  
245 distribution data as follows. For each SMPS scan, the particle size distribution is integrated  
246 backward starting from the bin with the largest-size particles – which corresponds to CCN with  
247 the lowest critical supersaturation,  $S_{cr}$ . We then successively add bins with smaller and smaller  
248 diameters, until the aerosol number matches the CCN concentration observed for the same time  
249 period as the SMPS scan. The particles in the smallest size bin, which we call *critical dry*  
250 *diameter*,  $D_{cr}$ , correspond to CCN with highest ~~critical supersaturation~~  $S_{cr}$  possible – being the  
251 instrument supersaturation,  $SS$ . From  $D_{cr}$  and  $SS$  we determine  $\kappa$  from Köhler theory (~~Petters~~  
252 ~~and Kreidenweis, 2007~~) [Petters and Kreidenweis, 2007](#)), assuming the particle chemical  
253 composition is internally mixed:



$$\kappa = \frac{4A^3}{27D_{cr}^3SS^2} \quad (1)$$

254 where  $A = \frac{4M_w\sigma_w}{RT\rho_w} \frac{4M_w\sigma}{RT\rho_w}$  is the Kelvin parameter, while  $M_w$  ( $\text{kg mol}^{-1}$ ),  $\sigma_w$  ( $\text{J m}^{-2}$ ) and  $\rho_w$  ( $\text{kg m}^{-3}$ ) are, respectively, the molar mass of water,  $\sigma$  ( $\text{J m}^{-2}$ ) is the surface tension and density of water/the solution droplet,  $R=8.3145 \text{ J mol}^{-1}\text{K}^{-1}$  is the universal gas constant and  $T$  (K) is the ambient temperature. Here we assume the surface tension of the solution droplet is equal to that of pure water ( $\sigma = \sigma_w$ ) by convention. The  $\kappa$  determined above represents the composition of particles with diameter  $D_{cr}$  (large particles can have a different  $\kappa$  but still activate given that their critical supersaturation  $S_{cr}$  is lower than the prevailing  $SS$  in the CCN chamber). This means that over the course of an hour, over which a full  $SS$  cycle is completed,  $\kappa$  is determined for a range of  $D_{cr}$ , which in our case were in the range of 50-200 nm (Section 3.1). This size-resolved  $\kappa$  information provides insights on the possible origin and chemical components of the aerosol, which is important given that there is no other measurement available to constrain chemical composition during RACLETs. From  $\kappa$ , we infer an equivalent organic mass fraction,  $\epsilon_{org}$ , assuming that the aerosol is composed of an organic-inorganic mixture:

$$\epsilon_{org} = \frac{(\kappa - \kappa_i)}{(\kappa_o - \kappa_i)} \quad (2)$$

267 where  $\kappa_i = 0.6$  and  $\kappa_o = 0.1$  are characteristic hygroscopicity values for the inorganic fraction of aerosol (represented by ammonium sulphate), and aged organics/organic aerosol, respectively (Petters and Kreidenweis, 2007; Wang et al., 2008; Dusek et al., 2010). Note that these values for a continental aerosol are supported by observations and analyses (e.g., Andreae and Rosenfeld, 2008; Rose et al., 2008; Pringle et al., 2010).

272

### 273 2.3 Cloud droplet number and cloud maximum supersaturation

274 Here we apply adiabatic cloud parcel theory to the observational datasets to determine the maximum in-cloud supersaturation ( $S_{max}$ ) and cloud droplet number ( $N_d$ ) that would form over both measurement sites throughout the observation period. Droplet calculations are carried out with the physically based aerosol activation parameterization of Nenes and Seinfeld (2003), with extensions introduced by Fountoukis and Nenes (2005), Barahona et al. (2010), and Morales and Nenes (2014). Each  $N_d$  calculation requires knowledge of the observed pressure, temperature, vertical winds, aerosol size distribution and hygroscopicity. For the WFJ site, all data are available as described in the sections above. For the WOP site, CCN (hence

282 hygroscopicity) data are not available, so we carry out  $N_d$  calculations at two  $\kappa$  values, 0.1 and  
283 0.25, which is the upper and the lower limit determined from the WFJ analysis (Section 3.1).  
284 The ability to reproduce observed cloud droplet number concentrations (“Method evaluation”,  
285 Section 3.2.1) further supports the selection of these values.

286 ~~Vertical velocity~~ The wind lidar measurements conducted at WOP (Section 2.1.4) are  
287 ~~obtained from the wind lidar data used to determine the prevailing vertical velocities at both~~  
288 ~~sites. Data extracted for from the altitude first bin of interest the lidar, being 200 m and 1100 m~~  
289 ~~AGL for WOP and WFJ, respectively. The measured updraft velocities AGL, are~~  
290 ~~then considered representative for WOP as the wind lidar has no values very close to the ground,~~  
291 ~~while measurements extracted for 1100 m AGL are used as a proxy for the vertical velocities~~  
292 ~~at WFJ. The high resolution wind lidar data are grouped by hour and each fitted to a half-~~  
293 Gaussian probability density ~~function (PDF) functions (PDFs)~~ with zero mean and standard  
294 deviation  $\sigma_w$ . ~~PDFs are obtained for An hourly segments, while an example of this calculation~~  
295 ~~method PDF of updraft velocities~~ is provided in the supplementary material ~~as an example of~~  
296 ~~the calculation method we followed here~~ (supplement Fig. S2). Employing the “characteristic  
297 velocity” approach of Morales and Nenes (2010), the PDF-averaged values of  $N_d$  and  $S_{max}$  are  
298 calculated by applying the parameterization using a single characteristic velocity,  $w^* = 0.79\sigma_w$ .  
299 This approach has been shown to successfully predict cloud-scale values of  $N_d$  in field studies  
300 for cumulus and stratocumulus clouds (e.g., Conant et al., 2004; Meskhidze et al., 2005;  
301 Fountoukis et al., 2007; Morales et al., 2014; Kacarab et al., 2020). The droplet closure carried  
302 out in this study is also used to support the validity of this approach for Alpine MPCs. To  
303 determine the  $\sigma_w$  values used in the closure study (Section 3.2.1), we isolated the segments of  
304 the wind lidar measurements that correspond to each cloud event observed by the Holoballoon  
305 platform. The subsequent fitting of the measured updraft velocities to half-Gaussian PDFs  
306 revealed a  $\sigma_w$  value representative of each cloud. The accuracy of the wind lidar products is  
307 affected by precipitation, as the measured updraft velocities might be masked by the terminal  
308 fall velocity of the hydrometeors. We therefore exclude precipitating periods from our analysis  
309 – using disdrometer measurements to constrain periods of precipitation. Aiming to examine  
310 how  $N_d$  responds to different vertical velocity-aerosol situations, as a sensitivity test, potential  
311  $N_d$  for both sites are calculated at 10 values of  $\sigma_w$  between 0.1 and 1.0  $\text{ms}^{-1}$  that cover the  
312 observed range (Section 3.2.4). Note that we use the term “potential” droplet number  
313 throughout this study, as its calculation is performed regardless of the actual existence of clouds  
314 over the measurement sites.

315

Formatted: Pattern: Clear (Background 1)

Formatted: Pattern: Clear (Background 1)

Formatted: Pattern: Clear (Background 1)

### 3. Results & Discussion and discussion

#### 3.1 Particle number, CCN concentration and $\kappa$ at WOP and WFJ

The total aerosol number concentration ( $N_{aer}$ ) timeseries (integrated aerosol size distribution) together with horizontal wind speed and direction measurements are depicted for both sites in Figure 1. The  $N_{aer}$  data points of WFJ are colored by  $\kappa$  (Section 2.2), while the orange dots are solid line is used as a trace for WOP timeseries, as  $\kappa$  was not determined for the site owing to a lack of corresponding CCN measurements. Aiming to interpret the aerosol variations and the potential differences observed between valley and high-altitude measurements, the two-week period of interest is divided into two different sub-periods. During 24 and 28 of February, a high-pressure system was dominant over Europe with clear skies and elevated temperatures (supplement Fig. S3). During this first sub-period, the  $N_{aer}$  varies considerably, and tends to follow a diurnal cycle that anticorrelates between the two sites (Fig. 1a). The concentrations at WOP are most of the times elevated with respect to WFJ, which is expected as the  $N_{aer}$  in the valley is higher – being influenced by local sources, which during this time of the year include emissions from biomass burning (BB) (Lanz et al., 2010).  $N_{aer}$  at WOP peaks in the evening, reaching up to  $\sim 10^4 \text{ cm}^{-3}$  presumably because of BB emissions in the valley which seem to stop around midnight (Fig. 1a). Up to 2 orders of magnitude lower  $N_{aer}$  is measured at the same time at the WFJ site. In the afternoon, aerosol numbers concentrations at WFJ approach those observed at WOP, indicating that the two sites are possibly experiencing similar air masses. The  $\kappa$  for WFJ seems to follow a clear temporal pattern as well, ranging between  $\sim 0.1$ - $0.4$  with a minimum in the afternoon, when the two sites experience the same air masses. Low  $N_{aer}$  values are accompanied by higher  $\kappa$ , while at higher  $N_{aer}$  conditions less hygroscopic aerosols are recorded (Fig. 1a).

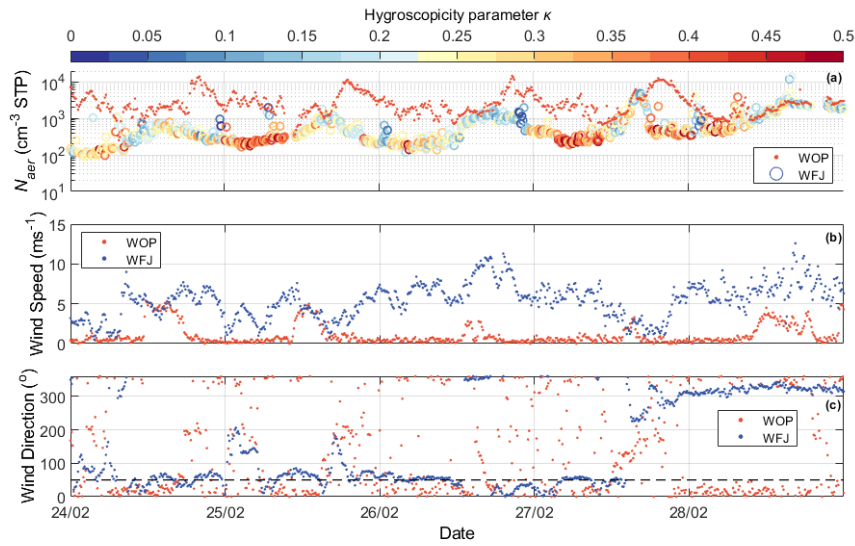
The above diurnal cycles and their relationships can be understood in terms of boundary layer dynamics typically occurring in mountain-valley systems (Chow et al., 2013). During daytime, under clear sky conditions, the slopes and the valley itself are warmed by solar radiation, causing rising of the BL, and additionally the production of buoyant air masses that rise up the slope toward the summit (through “up-slope” and “up-valley” winds) (Okamoto and Tanimoto, 2016). This hypothesis can be further supported by the fair weather recorded by the weather station at WFJ until 28 February (supplement Fig. S3). The buoyant upslope flow could then transport polluted air masses originating from the BL of the valley up to the WFJ site, elevating the concentrations of less hygroscopic aerosols observed in the afternoon. The situation reverses during nighttime, when cold air descends from the slopes (down-slope winds)

349 and flows out of the valley (down-valley winds) due to the radiative cooling of the surface. The  
350 less polluted air observed during the early hours of the day before sunrise indicates that the  
351 WFJ station remained in the free troposphere (FT), with lower  $N_{aer}$  and more aged air (i.e.  
352 ~~larger  $\kappa$ ) with a more prominent accumulation mode (Seinfeld and Pandis, 2006).~~larger  $\kappa$ ) with  
353 a more prominent accumulation mode (Baltensperger et al., 1997; pp. 376-378 in Seinfeld and  
354 Pandis, 2006; Kammermann et al., 2010; Jurányi et al., 2011).

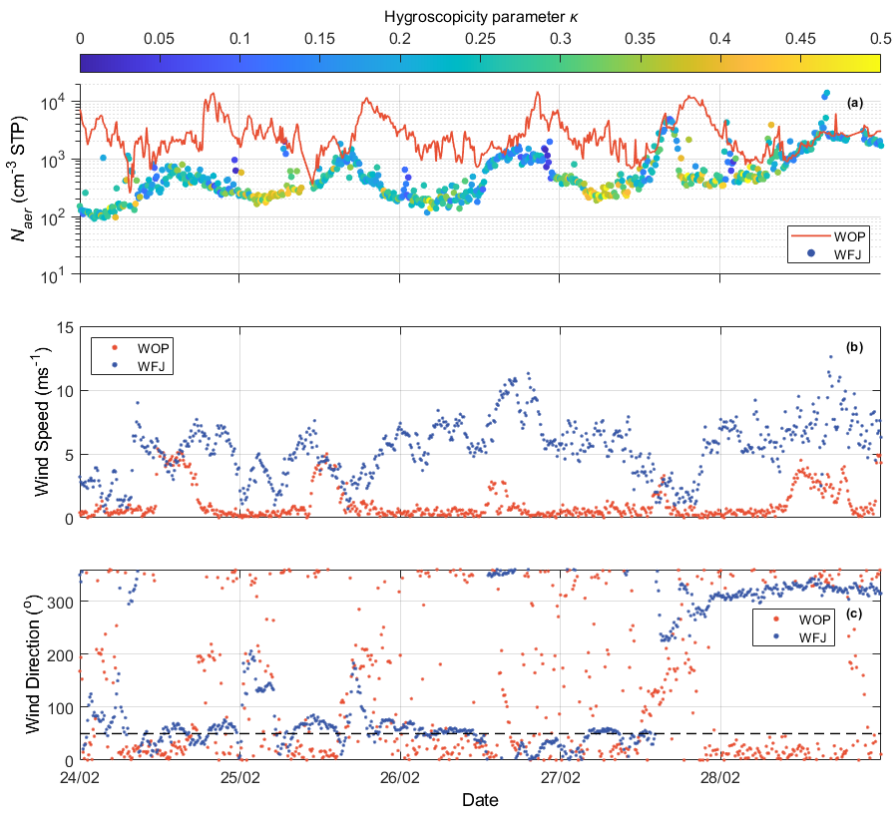
355 Another consideration is that the upslope flow that “connects” the valley and the  
356 mountain-top site may not only be driven by thermal convection but also from mechanically-  
357 forced lifting. The latter mechanism is caused by the deflection of strong winds by a steep  
358 mountain slope and it can be of great importance depending mainly on the height of the  
359 mountain and the mean speed of the wind (Kleissl et al., 2007). The local wind effects can be  
360 further interpreted looking at the MeteoSwiss timeseries of wind speed and direction for both  
361 stations (Fig. 1b, c). Wind measurements at WFJ station recorded a strong wind speed reaching  
362 up to  $\sim 11 \text{ ms}^{-1}$  from easterly-northeasterly directions between 24 and 28 of February. The wind  
363 direction measured at WFJ coincides with the relative location of WOP site (see black dashed  
364 line in Fig. 1c). The steep orography over the Alps would transform part of this strong  
365 horizontal motion into vertical motion, and transport air from WOP to WFJ, as seen in other  
366 Alpine locations, like Jungfrauoch (e.g., Hoyle et al., 2016). A detailed analysis however is  
367 out of the scope of this study.

368

369



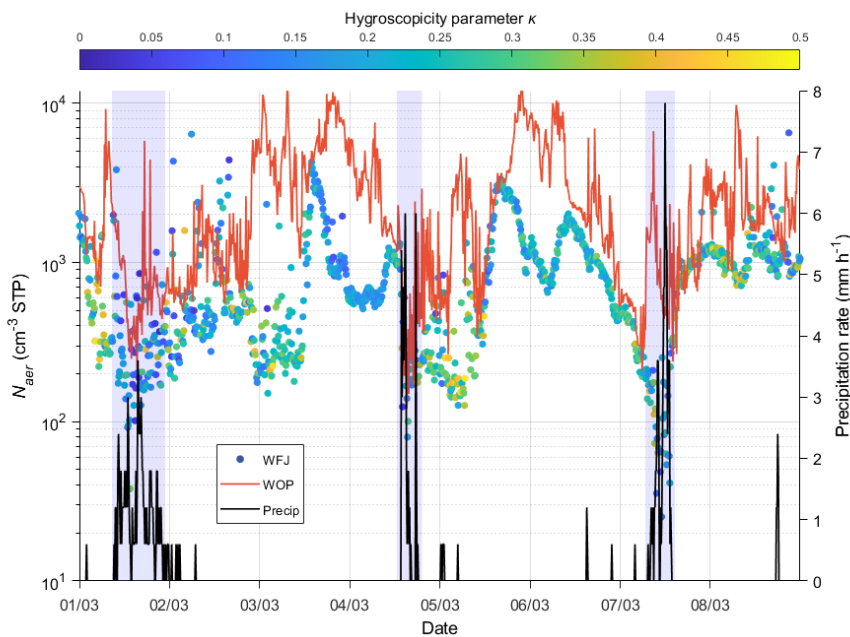
370



371 **Figure 1.** (a)  $N_{aer}$  in standard temperature and pressure conditions ( $\text{cm}^{-3}$  STP) at WOP (orange  
 372 dots) and at WFJ (circles colored by  $\kappa$ ), (b) wind speed ( $\text{ms}^{-1}$ ), and (c) wind direction (in  
 373 degrees) obtained from the MeteoSwiss observation stations at WFJ (blue dots) and Davos  
 374 (orange dots) between 24 and 28 February 2019. The black dashed line indicates the relative  
 375 direction of WOP to WFJ. Each day is referenced to 00 UTC.

376

377



378

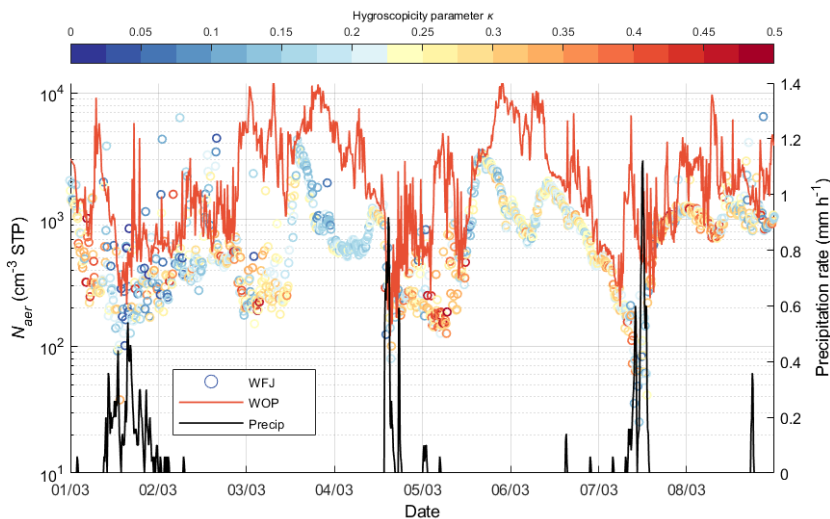
379 **Figure 2.**  $N_{aer}$  ( $\text{cm}^{-3}$  STP) at WOP (orange line) and at WFJ (circles colored by  $\kappa$ ). The black  
 380 solid line represents the precipitation rate ( $\text{mm h}^{-1}$ ) recorded from the MeteoSwiss observation  
 381 station for each 10-min interval at WFJ between 1 and 8 of March 2019. Focusing on the The blue-  
 382 shaded areas represent the periods when precipitation recorded at WFJ site is most intense.

383

384

385 Similar to Figure 1a, Figure 2 illustrates the  $N_{aer}$  timeseries measured at both sites along  
 386 with the precipitation rate recorded by the MeteoSwiss station at WFJ during the time period  
 387 between 1 and 8 March, meteorological 2019. Meteorological observations show the pressure  
 388 and temperature dropping (supplement Fig. S3) together with intense snow and rain events,  
 389 associated with the passage of cold fronts over the region. Three intense precipitation events  
 390 are visible in our dataset occurring on the 1<sup>st</sup>, 4<sup>th</sup> and 7<sup>th</sup> of March 2019 (blue-shaded areas on  
 391 Fig. 2) creating up to  $\sim 7.8$  mm per hour of precipitation (Fig. 2). The most intense drop in  $N_{aer}$   
 is seen to occur during and after the precipitation events, with the aerosol concentrations

392 dropping to less than  $200 \text{ cm}^{-3}$  ( $100 \text{ cm}^{-3}$ ) at WOP (WFJ). This is not the case for the last event,  
 393 where a big “spike” of  $N_{aer}$  is observed before the precipitation event in WOP timeseries, which  
 394 is in contrast with the concurrent sharp decrease in  $N_{aer}$  ( $< 20 \text{ cm}^{-3}$ ) observed at WFJ. This  
 395 could be an indication of a local source affecting the  $N_{aer}$  recorded in the valley. During dry  
 396 weather conditions, we can notice again the aerosol timeseries correlating during the afternoon  
 397 and anticorrelating later in the evening-early morning hours. On ~~the 3<sup>rd</sup> of March 3~~, a steep  
 398 increase in  $N_{aer}$  is seen in WFJ timeseries reaching up to  $\sim 4000 \text{ cm}^{-3}$ , which is followed by a  
 399 period of several hours with low hygroscopicity values ( $\kappa \ll 0.2$ ) indicating once more the  
 400 influence of freshly emitted particles arriving at WFJ from the BL of lower altitudes.  
 401 Additionally, between 1 and 8 March, the diurnal cycle of particle hygroscopicity is less  
 402 pronounced ~~compared to the period between 24 and 28 February~~. Especially on ~~the 1<sup>st</sup> and 7<sup>th</sup>~~  
 403 of March ~~nucleation processes or precipitation scavenging removes the more, less~~ hygroscopic  
 404 aerosols ~~from WFJ, thus leaving behind the ( $\kappa < 0.1$ ) - hence~~ less effective CCN particles  
 405 ~~characterized-~~ are found at WFJ (Fig. 2). This is likely from either ~~precipitation removing~~  
 406 ~~aerosol through diffusive and impaction processes, or, the removal of aerosol particles that first~~  
 407 ~~activate and then are removed by lower  $\kappa$  values ( $< 0.1$ )-precipitation~~. Also, because  $N_{aer}$  drops,  
 408 fresh local emissions become more important, further justifying the predominance of low  
 409 hygroscopicity values.



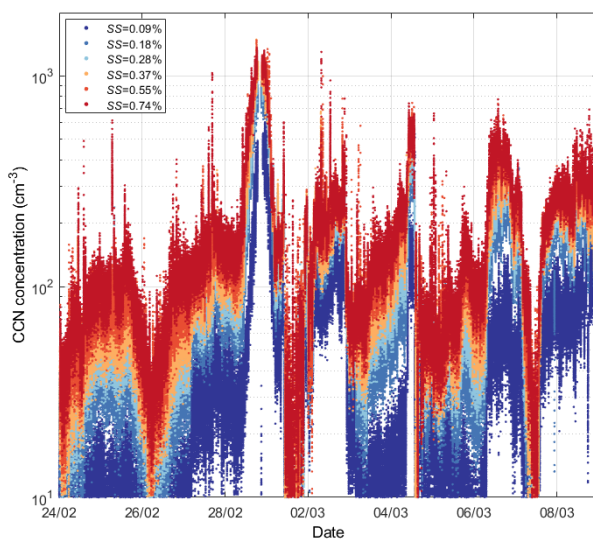
410 **Figure 2.**  $N_{aer}$  ( $\text{cm}^{-3}$  STP) at WOP (orange solid line) and at WFJ (circles colored by  $\kappa$ ). The  
 411 black solid line represents the precipitation rate ( $\text{mm h}^{-1}$ ) recorded from the MeteoSwiss  
 413 observation station for each 10 min interval at WFJ between 1 and 8 of March 2019.

414  
415 Figure 3 presents the CCN number concentration timeseries measured at ambient  
416 conditions at WFJ for all 6 supersaturations ~~measured~~. Throughout the two-week measurement  
417 period the recorded CCN number concentrations do not seem to follow a clear temporal pattern.  
418 The absence of a diurnal cycle in CCN properties measured at Jungfraujoch during winter was  
419 also pointed out in the study of Jurányi et al. (2011), because the site is mainly in free  
420 tropospheric conditions during most of the winter. According to Figure 3, the observed CCN  
421 concentrations tend to be low ( $\sim 10^2 \text{ cm}^{-3}$ ) even at the highest SS (0.74%), which is expected  
422 given that WFJ is a remote continental measurement site with CCN concentrations that are  
423 typical of ~~FF~~free tropospheric continental air (Jurányi et al., 2010, 2011; Hoyle et al., 2016;  
424 Fanourgakis et al., 2019). This is again in line with the measured monthly median values of  
425 CCN (at  $SS = 0.71\%$ ) reported by Jurányi et al. (2011) being equal to 79.1 and  $143.4 \text{ cm}^{-3}$  for  
426 February and March 2009, respectively. Some local CCN spikes are however recorded during  
427 the evening of 28 February and at the beginning of March (e.g., on 2<sup>nd</sup>, 4<sup>th</sup> and 6<sup>th</sup> March), with  
428 the observed values of CCN reaching up to  $650 \text{ cm}^{-3}$  at  $SS=0.09\%$  (lowest SS) and  $1361 \text{ cm}^{-3}$   
429 at  $SS=0.74\%$  (highest SS). Considering that WFJ is a site frequently located in the FT, sudden  
430 fluctuations in the CCN concentrations could be related to the vertical transport of freshly  
431 emitted particles (e.g., wood burning or vehicle emissions) from the valley floor in Davos. It is  
432 also worthy to note that some aerosol spikes observed on the 3<sup>rd</sup> ( $\sim 3350 \text{ cm}^{-3}$ ) and the 5<sup>th</sup> of  
433 March ( $\sim 2100 \text{ cm}^{-3}$ ) in the WFJ timeseries (Fig. 1a) are not accompanied by a corresponding  
434 peak in the CCN timeseries. This indicates the presence of small aerosol particles, which  
435 activate above 0.74% supersaturation (i.e. particles with a diameter smaller than ~~approx.  $\sim$~~  25  
436 nm). This event could also be associated with new particle formation (NPF) events. A previous  
437 study by Herrmann et al. (2015) reported the aerosol number size distribution at the  
438 Jungfraujoch over a 6-year period indicating that NPF was observed during 14.5% of the time  
439 without a seasonal preference. Tröstl et al. (2016) also showed that NPF significantly adds to  
440 the total aerosol concentration at Jungfraujoch and is favored only under perturbed FT  
441 conditions (i.e. BL injections). Finally, during the three intense precipitation events (on 1<sup>st</sup>, 4<sup>th</sup>  
442 and 7<sup>th</sup> March) we can identify again that the wet removal of the more hygroscopic aerosol  
443 (Fig. 2) suppresses the presence of cloud-activating particles, at times depleting the atmosphere  
444 almost completely from CCN (Fig. 3). This is clearly shown on the 1<sup>st</sup> and the 7<sup>th</sup> of March,  
445 when the CCN number measured at 0.74% supersaturation drops below  $10 \text{ cm}^{-3}$ , which is  
446 extremely low for BL concentrations.

Formatted: Font: Cambria Math



447 The aerosol hygroscopicity parameter derived from all CCN data collected between 24  
448 of February and 8 of March is presented in Figure 4a. The red solid line represents the hourly  
449 averaged hygroscopicity values over one complete instrument supersaturation cycle. The  
450 hygroscopic properties of the particles at WFJ vary as a function of supersaturation, exhibiting  
451 on average lower values ( $\sim 0.1$ ) at high  $SS$  and higher values ( $\sim 0.3$ ) at the lower  $SS$ . Since the  
452 supersaturation inversely depends on particle size, Figure 4a indicates that the hygroscopicity  
453 of the particles drops by almost 60% as the particles are getting smaller (i.e. as the  
454 supersaturation increases). Table 2 summarizes the mean values of  $\kappa$  and  $D_{cr}$  and their standard  
455 deviations, as calculated for each measured  $SS$ . The anticorrelation seen between the instrument  
456  $SS$  and  $D_{cr}$  is reasonable, if we consider that the latter represents the minimum activation  
457 diameter in a population of particles, and therefore only the particles with a  $D_{cr} > 193.54$  nm  
458 are able to activate into cloud droplets at low  $SS$  values (0.09%). The hourly averaged  
459 hygroscopicity at each  $SS$  slot falls within a range of  $\sim 0.2$  and  $\sim 0.3$ , which is a well  
460 representative value for continental aerosols (Andreae and Rosenfeld, 2008; Rose et al.,  
461 2008).



462 **Figure 3.** Timeseries of CCN number concentrations ( $\text{cm}^{-3}$ ) at WFJ for different levels of  
463 supersaturation ( $SS$ ) with respect to water between 24 February and 8 March 2019.  
464

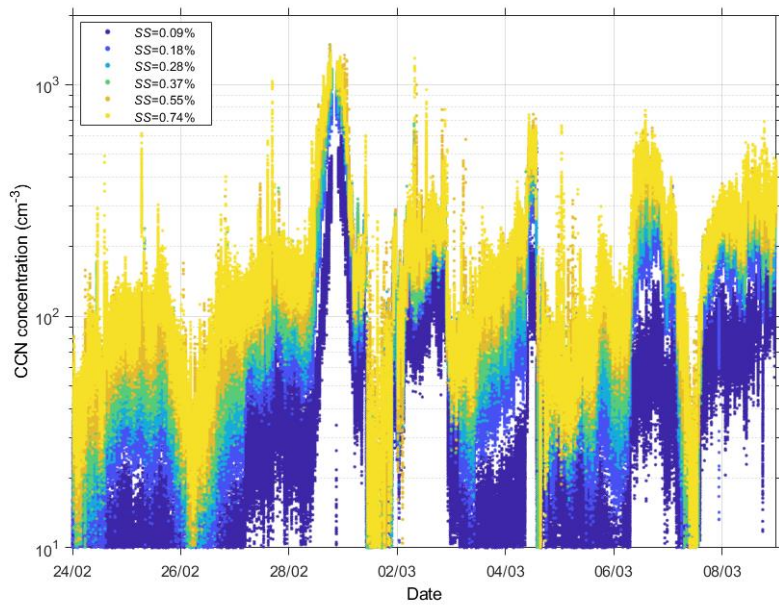
465

466 **Table 2.** Average  $\kappa$  and  $D_{cr}$  values at WFJ for each SS measured ~~over the period of~~  
467 ~~interest between 24 February and 8 March 2019.~~ Uncertainty for each value is expressed by  
468 the standard deviation.

<i>SS (%)</i>	<i><math>\kappa_{mean}</math></i>	<i><math>D_{cr,mean}</math></i>
0.09	$0.26 \pm 0.10$	$193.54 \pm 29.58$
0.18	$0.31 \pm 0.13$	$116.80 \pm 22.20$
0.28	$0.25 \pm 0.13$	$96.69 \pm 21.62$
0.37	$0.24 \pm 0.13$	$82.67 \pm 20.93$
0.55	$0.20 \pm 0.12$	$68.30 \pm 20.95$
0.74	$0.19 \pm 0.11$	$58.11 \pm 17.54$

469

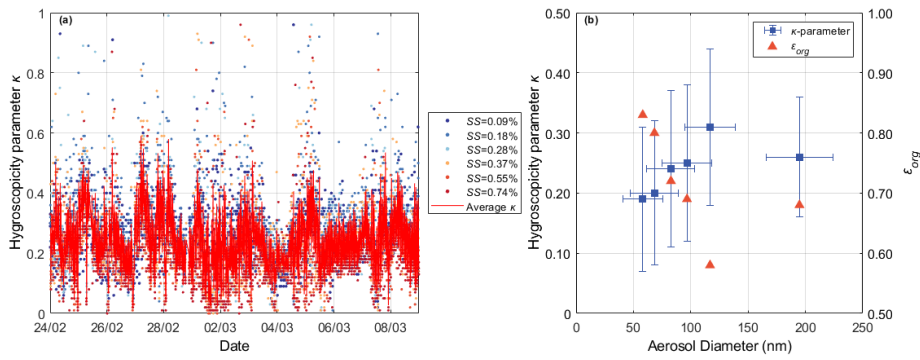
Formatted: Indent: First line: 0.47"



470

471

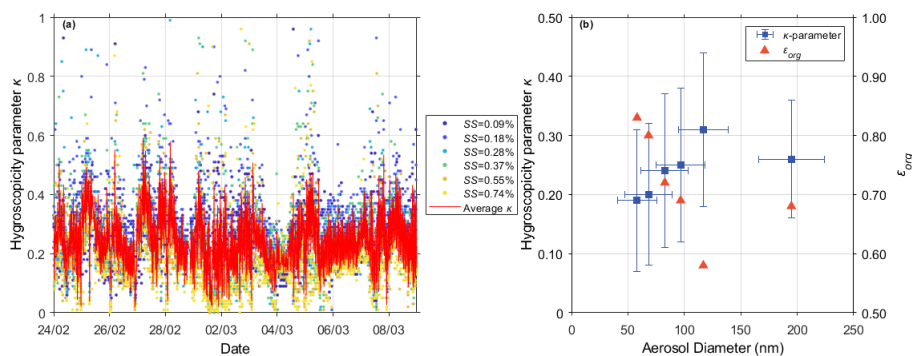
**Figure 3.**



472

473 Timeseries of in-situ CCN number concentrations ( $\text{cm}^{-3}$ ) at WFJ for different levels of  
 474 supersaturation (SS) with respect to water between 24 February and 8 March 2019.

475



476  
 477 **Figure 4.** (a) Timeseries of the hygroscopicity parameter  $\kappa$  at WFJ at different levels of  
 478 instrument supersaturation (0.09–0.74%) throughout the period of interest. The solid red line  
 479 indicates the hourly averaged  $\kappa$  timeseries over a complete SS cycle. (b) Size-resolved aerosol  
 480 hygroscopicity (blue squares) and the respective  $\epsilon_{org}$  (orange triangles) calculated for the WFJ  
 481 site.

482  
 483 The hygroscopicity parameter along with the inferred  $\epsilon_{org}$  (Eq. 2) is shown in Figure 4b  
 484 as a function of particle size. Compared to smaller particles, the higher  $\kappa$  of larger particles  
 485 (>100 nm) is consistent with them being more aged and with a lower fraction of organics. The  
 486 smaller particles are possibly enriched in organic species, which is consistent with the notion  
 487 that airmasses in the valley can contain large amounts of freshly emitted BB smoke with lower  
 488  $\kappa$ . Aerosol particles in the FT are considerably more aged ([pp. 376-378 in Seinfeld and Pandis,](#)  
 489 2006) and exhibit higher values of  $\kappa$  and consequently lower values of  $\epsilon_{org}$ . The chemical  
 490 composition of sub-100 nm particulate matter was therefore presumably dominated by organic  
 491 material transported from the valley, while the higher  $\kappa$  values characterizing the larger  
 492 particles are consistent with the more aged character of free tropospheric aerosols (e.g., Jurányi  
 493 et al., 2011). The higher  $\epsilon_{org}$  inferred for the smaller particles suggests that mixing between  
 494 fresh emissions in the valley and the free tropospheric aerosol might also be taking place at  
 495 WFJ.

496  
 497 3.2 Potential cloud droplet number concentration and maximum supersaturation  
 498 3.2.1 Method evaluation

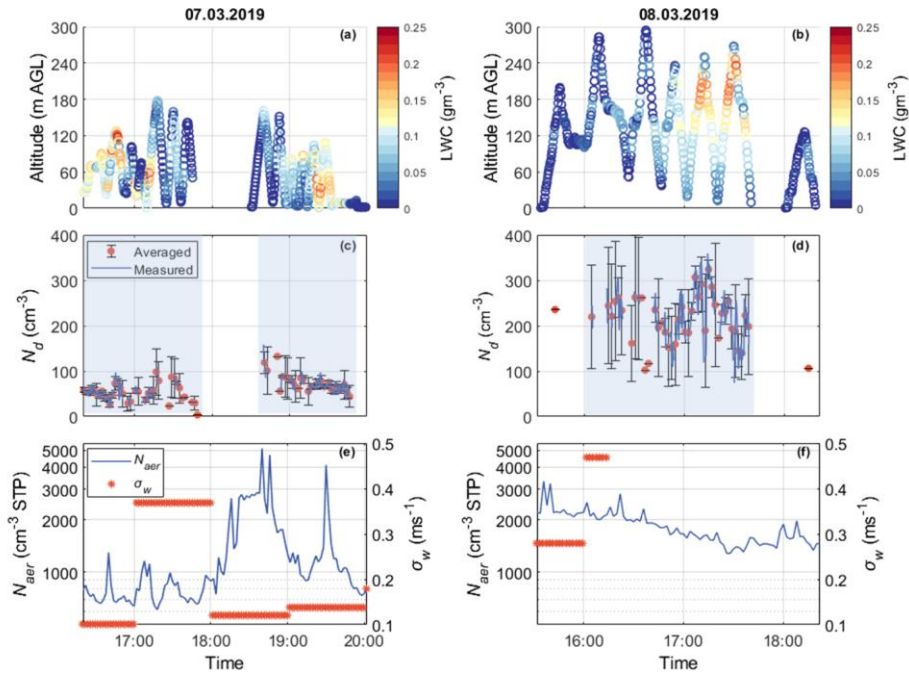
499 [Figure 5 presents an overview of each measurement carried out by the HoloBalloon. During the](#)  
 500 [RACLETS campaign, planar and dendritic ice particles were collected from supercooled](#)  
 501 [clouds at WFJ aiming to examine their refreezing ability. A detailed description of the sampling](#)

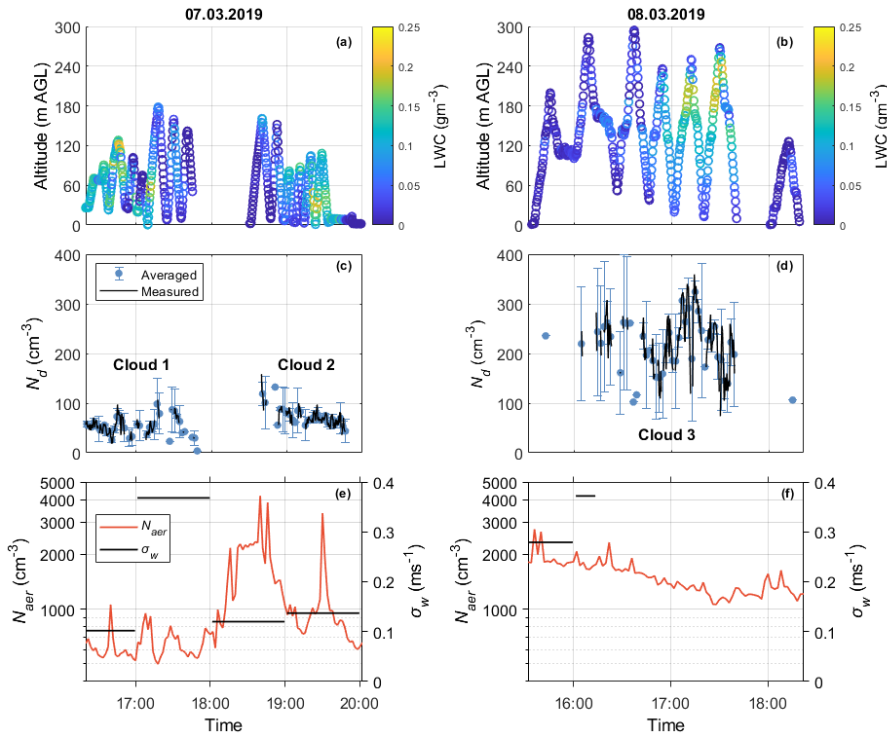
502 methodology can be found in Mignani et al. (2019). Between March 1 and March 7, images of  
503 single dendrites were taken and analyzed visually for the degree of riming (supplement Fig.  
504 S4). The estimated riming degree varies from 1 (lightly-rimed) to 4 (heavily-rimed) following  
505 the categorization of Mosimann et al. (1994). Some representative images of each measured  
506 riming degree are shown in Figure S4b. Although images were captured intermittently, they  
507 were taken within all three intense precipitating events occurring during the period of interest  
508 (blue-shaded areas on Fig. 2). All dendrites captured were at least lightly rimed (i.e. riming  
509 degree = 1), which provides direct evidence for the co-existence of supercooled droplets and  
510 ice in clouds. Except the indirect evidence of the presence of MPCs over WFJ, Figure 5  
511 provides an overview of the direct microphysical measurements carried out by the Holoballoon  
512 at WOP (Section 2.1.3). Three cloud events are sampled during the 7<sup>th</sup> and the 8<sup>th</sup> of March, a  
513 more detailed description of which can be found in Ramelli et al. (2020b, c). The observed  
514 low-level clouds are likely produced by orographic lifting when the low-level flow is forced to  
515 ascent over the local topography from Klosters to WOP producing local updrafts and thus water  
516 supersaturated conditions. ~~The potential droplet formation is evaluated using the updraft~~  
517 ~~velocities PDF calculated for each cloud period (Section 2.3). On March 8, the disdrometer~~  
518 ~~recorded rainfall over WOP, starting a few minutes after the development of the observed cloud~~  
519 ~~system reflected in the gap of updraft velocity timeseries (Fig. 5f). In this case, to determine~~  
520 ~~the relevant updraft velocity from the wind lidar measurements, we focused on the 15-min time~~  
521 ~~period before the precipitation occurrence. The Gaussian fit to the updraft velocity gave a~~  
522 ~~distribution with  $\sigma_w = 0.24$  and  $0.16 \text{ ms}^{-1}$  for the first two clouds present on the 7<sup>th</sup> of March,~~  
523 ~~and,  $\sigma_w = 0.37 \text{ ms}^{-1}$  for the cloud system observed on the 8<sup>th</sup> of March. The  $w^+$  values used to~~  
524 ~~apply the droplet parameterization are thus between  $0.1$ – $0.4 \text{ ms}^{-1}$  (Section 2.3).~~

525 The cloud LWC measurements from the holographic imager display significant temporal  
526 variability that is also related to variations in the altitude of the tethered balloon system, as it  
527 tends to follow an adiabatic profile (Fig. 5a, b). Deviations from the adiabatic LWC profile are  
528 likely caused by entrainment of dry air within the low-level clouds. Departures during the  
529 mixed-phase conditions recorded on March 8 (Fig. 5b), could also be attributed to the depletion  
530 of  $N_d$  through riming and depositional growth. These two processes are frequently found to  
531 enhance orographic precipitation in feeder clouds. Indeed, a large fraction of rimed ice particles  
532 and graupel were observed that day with HOLIMO between 17:00 and 17:40 UTC (Ramelli et  
533 al., 2020c). Throughout the two-day dataset presented in Figure 5, the HoloBalloon system  
534 samples at altitudes lower than 300 m AGL, providing observations that are representative of  
535 BL conditions.

536 The observed  $N_d$  timeseries collected at WOP are illustrated in Figures 5c and ~~45d~~ 5d. The  
537 measurements corresponding to  $LWC < 0.05 \text{ gm}^{-3}$  are filtered out from the analysis, assuming  
538 that they do not effectively capture in-cloud conditions. A similar criterion for LWC was also  
539 applied in ~~Lloyd et al. (2015)~~ Lloyd et al. (2015) to determine the periods when clouds were  
540 present over the Alpine station of Jungfraujoch. Since the measured cloud properties have finer  
541 resolution (10-20 secs) than the predicted ones, the observed dataset is averaged every 2  
542 minutes. On March 7, the balloon-borne measurements were taken in a post-frontal air mass  
543 (i.e. passage of a cold front in the morning) and indicated the formation of two low-level liquid  
544 layers (~~blue shaded areas in~~ Fig. 5c) over WOP, which is attributed to low-level flow blocking  
545 (Ramelli et al., 2020b). Note that small droplets ( $< 6 \mu\text{m}$ ) cannot be detected by HOLIMO  
546 (Section 2.3.1) and therefore the reported  $N_d$  should be considered as a lower estimate. The  
547 influence of small cloud droplets, however, on the reported LWC is minor, since the  
548 contribution of the larger cloud droplets dominates. During the first cloud event, an  $N_d$  of up to  
549  $\sim 100 \text{ cm}^{-3}$  was recorded, while slightly increased  $N_d$  in the range of  $\sim 50\text{-}120 \text{ cm}^{-3}$  is visible  
550 during the second cloud event. On March 8, a small-scale disturbance passed the measurement  
551 location Davos, which brought precipitation (Ramelli et al., 2020c). During the passage of the  
552 cloud system, the in-situ measurements collected at WOP revealed the presence of a persistent  
553 low-level feeder cloud confined to the lowest 300 m of the cloud. The mixed-phase low-level  
554 cloud that is shown in Figure 5d, turned into an ice-dominated low-level cloud after 18 UTC  
555 (not shown). Throughout this event,  $N_d$  seems to range between  $\sim 100\text{-}350 \text{ cm}^{-3}$  (Fig. 5d), while  
556 the observed ICNC was in the range of  $\sim 1\text{-}4 \text{ L}^{-1}$  (see Fig. 6b in Ramelli et al., 2020c).

557  
558





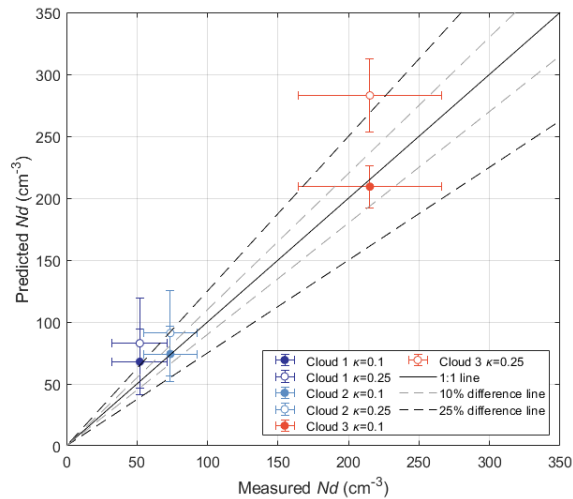
559  
 560 **Figure 5.** Timeseries of the 7<sup>th</sup> (left panels) and the 8<sup>th</sup> (right panels) of March, showing the  
 561 vertical profiles of the LWC ( $\text{gm}^{-3}$ ) in (a) and (b), the filtered (blue/black lines) and the 2-minute  
 562 average (orange dots/averaged (cyan circles)  $N_d$  ( $\text{cm}^{-3}$ ) measured at WOP with the HoloBalloon  
 563 platform in (c) and (d), and the corresponding SMPS aerosol concentrations ( $\text{cm}^{-3}$ -STP) (blue  
 564 (orange line) and the hourly wind-lidar derived  $\sigma_w$  values ( $\text{ms}^{-1}$ ) (orange stars/black line) in (e)  
 565 and (f). The blue shaded areas in (e) and (d) Error bars represent the three cloud events  
 566 observed, while error bars indicate the standard deviation of  $N_d$  during the averaging period.

567  
 568 According to Figures 5e and 5f, low  $N_{aer}$  ( $<10^3 \text{ cm}^{-3}$ ) and intermediate  $\sigma_w$  values are  
 569 representative of the period throughout which the first cloud formed, while up to 4 times higher  
 570  $N_{aer}$  is observed during the following two cloud events, with relatively low  $\sigma_w$  values  
 571 characterizing the second cloud compared to the third one. These On March 8, the disdrometer  
 572 recorded rainfall over WOP, starting a few minutes after the development of the observed cloud  
 573 system, reflected in the removal of updraft velocity measurements after 16:15 (Fig. 5f). Note  
 574 that the concentration measurements presented in Figure 5 correspond to ambient temperature  
 575 and pressure conditions. The contrasted aerosol and vertical velocity regimes, in which the  
 576 observed clouds are formed, offer a great opportunity to test how the proposed methodology

Formatted: Indent: First line: 0"



577 performs under a wide range of aerosol and velocity conditions. Indeed, the mean cloud droplet  
 578 diameters exhibit a wide range of values, which for WOP range between 10  $\mu\text{m}$  and 17  $\mu\text{m}$  on  
 579 March 7, and 8  $\mu\text{m}$  to 12  $\mu\text{m}$  on March 8 (not shown).



580  
 581 **Figure 6.** Comparison between average predicted  $N_d$  ( $\text{cm}^{-3}$ ) with the droplet activation  
 582 parameterization and  $N_d$  ( $\text{cm}^{-3}$ ) observed during the three cloud events on the 7<sup>th</sup> (blue and  
 583 cyan) and the 8<sup>th</sup> of March (orange) 2019. For all three cloud events droplet closure is  
 584 performed assuming a  $\kappa$  parameter of 0.1 (filled circle) and 0.25 (empty circle). The error bars  
 585 represent the standard deviation of  $N_d$  during each cloud event.

586  
 587 The  $N_d$  closure performed for the three cloud events observed over WOP during the last  
 588 two days of the period of interest is presented in Figure 6. TheNote that the potential droplet  
 589 formation is evaluated using the updraft velocity PDF calculated for each cloud period, rather  
 590 than the hourly  $\sigma_w$  data shown in Figures 5e and 5f (Section 2.3). Owing to the precipitation  
 591 occurrence during March 8, we focused on the 15-min time period between 16:00 and 16:15 to  
 592 determine a relevant updraft velocity from the wind lidar measurements representative of  
 593 Cloud 3. The Gaussian fit to the updraft velocities gave a distribution with  $\sigma_w = 0.24$  and  $0.16$   
 594  $\text{ms}^{-1}$  for the first two clouds present on the 7th of March, and,  $\sigma_w = 0.37 \text{ ms}^{-1}$  for the cloud  
 595 system observed on the 8th of March. The  $w^*$  values used to apply the droplet parameterization  
 596 are therefore between  $0.1\text{-}0.4 \text{ ms}^{-1}$  (Section 2.3). Figure 6 indicates that the parameterization  
 597 predictions agree to within 25% with the in-situ cloud droplet number concentrations. A similar  
 598 degree of closure is frequently obtained for other in-situ studies (e.g., Meskhidze et al., 2005;  
 599 Fountoukis et al., 2007; Morales et al., 2011; Kacarab et al., 2020), which however faced on

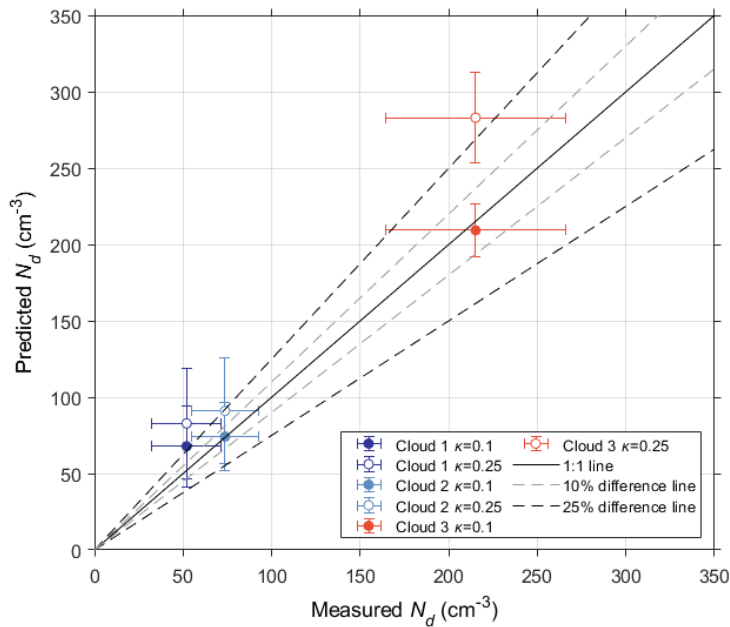
Formatted: Left, Line spacing: single

600 ~~liquid phase clouds. Here we show that the methodology can also work for mixed phase clouds~~  
601 ~~(i.e. Cloud 3 in Fig. 6).~~focused on liquid-phase clouds. Here we show that the methodology  
602 ~~can also work for MPCs (i.e. Cloud 3 in Fig. 6). It is important to note here that part of the~~  
603 ~~discrepancy between prediction and measurement could also be related to the underestimation~~  
604 ~~of the measured  $N_d$  (Section 2.1.3). Hence, an even better degree of closure is likely. The good~~  
605 ~~agreement between measurements and predictions - even under mixed-phase conditions,~~  
606 ~~reveals that processes like condensation freezing and the removal of cloud droplets through~~  
607 ~~riming and collision-coalescence are not disturbing the  $S_{max}$  and hence the  $N_d$  predicted by the~~  
608 ~~parameterization, at least for the given clouds. Pre-existing liquid and ice hydrometeors falling~~  
609 ~~to the examined cloud levels might also deplete the supersaturation affecting the number of the~~  
610 ~~activated droplets. The contribution of supersaturation depletion can readily be included in the~~  
611 ~~droplet activation parameterization (Sud et al., 2013; Barahona et al., 2014) but is not~~  
612 ~~considered in this study.~~ Furthermore, the parameterization predictions indicate that the best fit  
613 is achieved using a  $\kappa$  of  $\sim 0.1$ . ~~Aerosol concentrations (Fig. 6).  $N_{aer}$  at WOP are therefore is~~  
614 ~~likely~~ dominated by lower  $\kappa$  values, indicating that the particles are getting richer in organic  
615 material, compared to WFJ, which supports the aerosol analysis carried out in Section 3.1.  
616 These results are robust, indicating that for non-precipitating BL clouds the proposed  
617 calculation method captures cloud droplet formation at WOP and WFJ.

618

Formatted: English (United States)

Formatted: Justified, Indent: First line: 0.47", Line spacing: 1.5 lines



619  
 620 **Figure 6.** Comparison between average predicted  $N_d$  ( $\text{cm}^{-3}$ ) with the droplet activation  
 621 parameterization and  $N_d$  ( $\text{cm}^{-3}$ ) observed during the three cloud events on the 7<sup>th</sup> (blue and cyan  
 622 circles) and the 8<sup>th</sup> of March (orange circles) 2019. For all three cloud events droplet closure is  
 623 performed assuming a  $\kappa$  parameter of 0.1 (filled circles) and 0.25 (empty circles). The error  
 624 bars represent the standard deviation of  $N_d$  during each cloud event.

625  
 626 **3.2.2 Droplet formation at WOP and WFJ**

627 According to the methodology proposed in Section 2.3, using the in-situ measured aerosol  
 628 number size distribution  $N_{aer}$ , the estimated chemical composition and the observed updraft  
 629 velocity range, we determine the  $N_d$  and  $S_{max}$  that would form over both measurement sites.  
 630 WeAt WOP, clouds are formed locally due to the local topography (Ramelli et al., 2020b, c),  
 631 supporting the use of surface measured aerosol to estimate the potential  $N_d$  over this site. This  
 632 is further supported by the good degree of droplet closure (Section 3.2.1). A similar closure  
 633 study could not be repeated for WFJ owing to a lack of in-situ data, however the airmasses  
 634 sampled (i.e. those given as input to the parameterization) are often in the FT, so they should  
 635 contain the same aerosol as the one used to form the clouds. This does not apply under  
 636 perturbed FT conditions, which are however accompanied by the presence of less hygroscopic  
 637 particles over the mountain-top site and are less likely related to cloud formation (Section 3.1).  
 638 Here we assume a  $\kappa$  of 0.25 to calculate the potential droplets for WFJ according to our CCN-

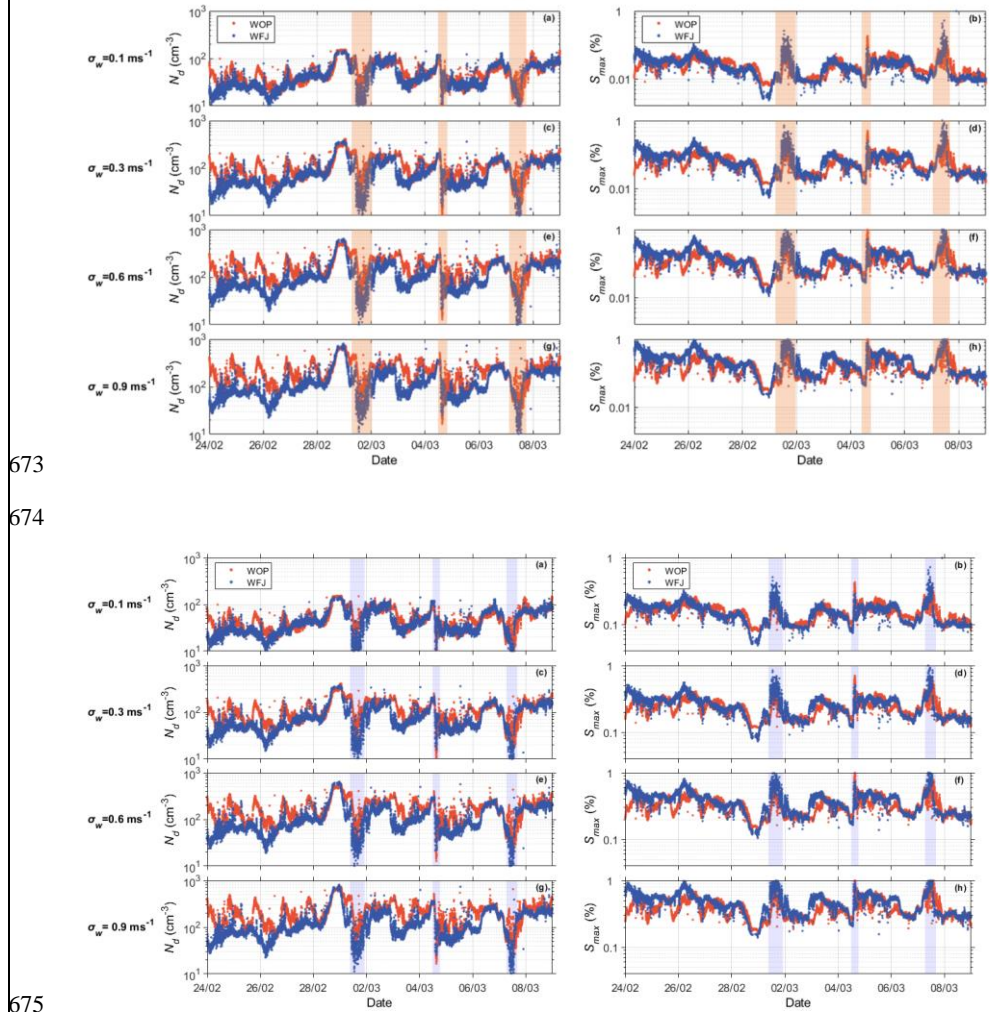
Formatted: Left, Line spacing: single

639 derived hygroscopicity values (Table 2) and given that  $S_{max}$  usually ranges between  $\sim 0.1$ - $0.3\%$ .  
640 In estimating the potential droplets for WOP, we use a  $\kappa$  of 0.1 given that aerosol is likely  
641 strongly enriched in organics; the good degree of closure that this value ~~provides~~ supports its  
642 selection (Section 3.2.1). Figure 7 depicts the potential  $N_d$  and the corresponding  $S_{max}$   
643 timeseries calculated at ambient conditions for WOP (orange dots) and WFJ (blue dots) using  
644 cloud updraft velocities that are indicative of the observed  $\sigma_w$  range, ~~being~~ (Section 3.4),  
645 namely 0.1, 0.3, 0.6 and 0.9  $\text{ms}^{-1}$ . The same behavior is seen for all four  $\sigma_w$  values selected  
646 while, as expected, larger values of  $N_d$  and  $S_{max}$  are achieved at higher  $\sigma_w$ . During the first days  
647 of the period of interest, the calculated  $N_d$  at WOP (Fig. 7a, c, e, g) is up to 10 times larger than  
648 at WFJ, despite the lower  $\kappa$  values characterizing its aerosol population. WFJ tends to have  
649 lower  $N_d$  due to the lower  $N_{aer}$  recorded. It is also important to highlight the anticorrelation  
650 between  $S_{max}$  and  $N_d$  values arising from the nonlinear response of droplet number and  
651 maximum cloud parcel supersaturation to fluctuations in the available aerosol/CCN  
652 concentrations (Reutter et al., 2009; Bougiatioti et al., 2016; Kalkavouras et al., 2019). Higher  
653  $N_{aer}$  elevates  $N_d$  values. The available condensable water is then shared among more growing  
654 droplets, depleting the supersaturation. Even more interesting is the fact that until February 28  
655 the calculated  $N_d$  timeseries at WOP show a pronounced diurnal cycle, similar to the total  $N_{aer}$   
656 timeseries (Section 3.1). Lower  $N_d$  values are visible during nighttime due to the limited  
657 turbulence. Droplet concentrations at WFJ do not follow a diurnal pattern in contrast to the  
658 aerosol data (Fig. 1a). However, the activation fraction (i.e.  $N_d/N_{aer}$ ) at WFJ displays a clear  
659 diurnal variability until the end of February (supplement Fig. ~~S3S5~~).

660 Through comparison with the MeteoSwiss precipitation measurements at WFJ (Fig. 4),  
661 it should be emphasized again that during the second sub-period of interest the occurrence of  
662 precipitation is followed by a depression in  $N_d$  (Fig. 7a, c, e, g) and a concurrent increase in  
663  $S_{max}$  reaching up to  $\sim 1\%$  (Fig. 7b, d, f, h). Especially at WFJ,  $N_d$  drops almost to zero on the  
664 1st, the 4th and the 7th of March, when precipitation is most intense (~~orange~~blue-shaded areas  
665 ~~on~~in Fig. 2 and 7). These trends are related to the washout of hygroscopic material observed at  
666 WFJ (Fig. 2) leading to the extremely low CCN concentrations ( $\sim 10 \text{ cm}^{-3}$ ) measured during  
667 these three days. During the first two intense precipitation events, the ~~aerosol concentrations~~  
668 ~~are~~ $N_{aer}$  is relatively high, compared to the third event, with concentrations reaching up to  $\sim 300$   
669  $\text{cm}^{-3}$  at both stations. The small activation fraction (supplement Fig. ~~S3S5~~) combined with the  
670 high  $S_{max}$  values indicates once more that small particles that activate into cloud droplets only

671 above 0.3 to 0.5% of supersaturation are present at both stations. However, this behavior is not  
 672 seen on March 7 for at WFJ.

Formatted: Highlight

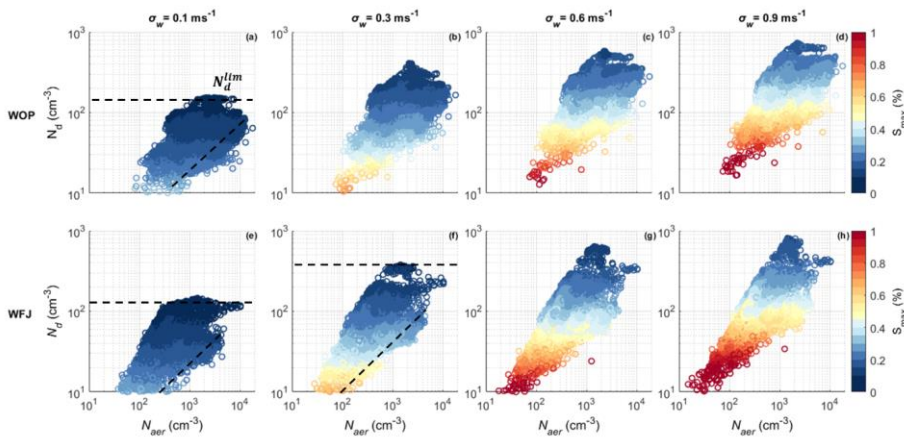


675  
 676 **Figure 7.** Calculated timeseries of  $N_d$  ( $\text{cm}^{-3}$ ) (left panels) and  $S_{max}$  (%) (right panels), for updraft  
 677 velocities of  $\sigma_w = 0.1 \text{ ms}^{-1}$  in a and b,  $0.3 \text{ ms}^{-1}$  in c and d,  $0.6 \text{ ms}^{-1}$  in e and f, and  $0.9 \text{ ms}^{-1}$  in g  
 678 and h, during the period of interest at WOP (orange dots) and WFJ (blue dots). The orangeblue-  
 679 shaded areas represent the intense precipitating periods when precipitation is recorded at WFJ  
 680 site, followed by a depression as shown in droplet number Figure 2.

681

682 3.2.3 Droplet behavior under velocity-limited conditions

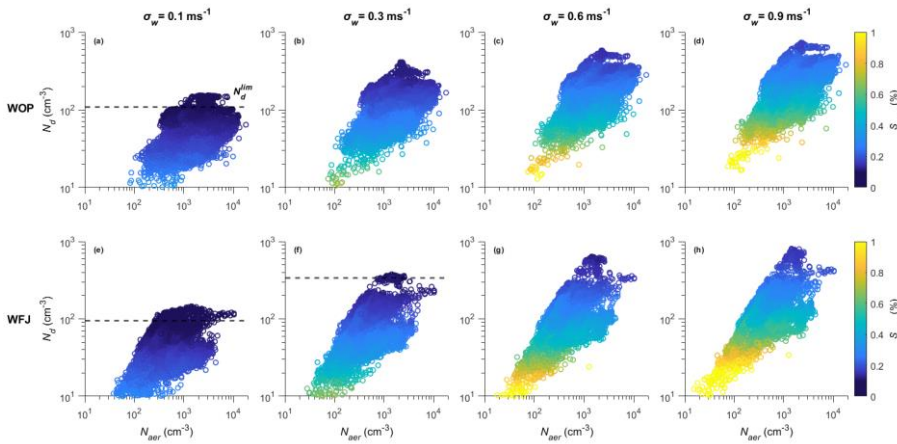
683 Combining the potential  $N_d$  and the corresponding  $S_{max}$  with the aerosol size distribution data,  
684 it is important to identify regimes where clouds formed are sensitive to vertical velocity  
685 changes or they are sensitive to variations in aerosol concentrations. Figure 8 shows the  
686 response of the calculated  $N_d$  to changes in total aerosol concentration for a representative range  
687 of updraft velocities prevailing over WOP (top panels) and WFJ (bottom panels). The data are  
688 colored by the respective  $S_{max}$  achieved in cloudy updrafts. For low  $\sigma_w$  values (Fig. 8a, d) we  
689 can identify that above an aerosol concentration of  $\sim 300 \text{ cm}^{-3}$ , the maximum  $N_d$  at both stations  
690 reaches a plateau, where its incremental change becomes insensitive to further aerosol changes.  
691 At WFJ, the same behavior is seen for intermediate  $\sigma_w$  values and  $N_{aer} \gtrsim 1000 \text{ cm}^{-3}$  (Fig. 8f).  
692 The horizontal dashed lines plotted on Figure 8 (a), (e) and (f) illustrate this plateau, which is  
693 termed limiting droplet number ( $N_d^{lim}$ ), following Kacarab et al. (2020).  $N_d^{lim}$  is reached owing  
694 to the extreme competition of the high aerosol concentrations for the available condensable  
695 water. In this regime, the clouds are insensitive to aerosol variations and the modulation of the  
696 droplet number is driven mostly by the cloud dynamics, hence the updraft velocity variability.  
697 Consequently, when  $N_d$  approaches  $N_d^{lim}$  the underlying dynamics control the cloud  
698 microphysics. Within the velocity-limited regime of droplet formation, we can notice that the  
699 corresponding  $S_{max}$  values are low ( $< 0.1\%$ ), reflecting the severe water vapor limitation that  
700 allows only a few particles to activate into cloud droplets. Conversely, when  $S_{max}$  in clouds  
701 exceeds  $0.1\%$  droplet formation in the BL of both measurement sites is always in the aerosol-  
702 limited regime, as the maximum supersaturation is high enough to activate almost all particles  
703 except for the very small ones. In the aerosol-limited regime,  $N_d$  never exceeds the  
704 characteristic limit,  $N_d^{lim}$ .



705  
706 Combining the potential  $N_d$  and the corresponding  $S_{max}$  with the  $N_{aer}$  data yields important  
707 information on whether clouds are sensitive to vertical velocity or aerosol changes. Cloud  
708 studies (e.g., Jensen and Charlson, 1984; Twomey, 1993; Ghan et al., 1998, Nenes et al., 2001  
709 and Reutter et al., 2009) have long recognized the role of water vapor competition on droplet  
710 formation, while the success of mechanistic parameterizations for climate models relies on the  
711 ability to capture this effect accurately (e.g., Ghan et al., 2011; Morales and Nenes, 2014).  
712 Twomey (1993) discusses this conceptually and states that competition may be fierce enough  
713 to reduce  $N_d$  with increasing  $N_{aer}$ , which was later demonstrated by Ghan et al. (1998) to occur  
714 for mixtures of sulfate aerosol and sea spray. Reutter et al. (2009) did not focus on such extreme  
715 conditions of water vapor competition, but rather situations that are consistent with dominance  
716 of anthropogenic pollution in clouds. Indeed, for high  $N_{aer}$ , droplets in clouds become  
717 insensitive to aerosol perturbations, giving rise to the so-called “velocity limited cloud  
718 formation”. Figure 8 displays this, presenting the response of the calculated  $N_d$  to changes in  
719  $N_{aer}$  for a representative range of updraft velocities prevailing over WOP (top panels) and WFJ  
720 (bottom panels). The data are colored by the respective  $S_{max}$  achieved in cloudy updrafts. For  
721 low  $\sigma_w$  values (Fig. 8a, d) we can identify that above an  $N_{aer}$  of  $\sim 300 \text{ cm}^{-3}$ , the  $N_d$  at both  
722 stations reaches a plateau, where it becomes insensitive to further aerosol changes. At WFJ,  
723 the same behavior is seen for intermediate  $\sigma_w$  values and  $N_{aer} \gtrsim 1000 \text{ cm}^{-3}$  (Fig. 8f). Kacarab et  
724 al. (2020) and Bougiatioti et al. (2020) examined a wide range of ambient size distributions  
725 and proposed that clouds became velocity-limited when  $S_{max}$  dropped below 0.1%. This reflects  
726 the increasingly fierce competition for water vapor during droplet formation, which allows only  
727 a few particles to activate into cloud droplets.



728



729

730 **Figure 8.** In-situ  $N_d$  ( $\text{cm}^{-3}$ ) vs.  $N_{aer}$  ( $\text{cm}^{-3}$ ), for updraft velocities of  $\sigma_w = 0.1 \text{ ms}^{-1}$  in a and e,  $0.3$   
 731  $\text{ms}^{-1}$  in b and f,  $0.6 \text{ ms}^{-1}$  in c and g and  $0.9 \text{ ms}^{-1}$  in d and h, during the period of interest at WOP  
 732 (top panels) and WFJ (bottom panels). Data are colored by  $S_{max}$  (%).

Formatted: Font: Not Bold

733

Formatted: Justified, Line spacing: 1.5 lines

734 Building upon these findings, we used the predicted  $S_{max}$  as an indicator for aerosol- or  
 735 velocity-limited conditions prevailing over the Alps. The horizontal dashed lines plotted on  
 736 Figure 8 (a), (e) and (f) illustrate a plateau, where  $S_{max} < 0.1\%$  and the modulation of the  $N_d$  is  
 737 driven mostly by the cloud dynamics, hence the updraft velocity variability, rather than aerosol  
 738 variations. This plateau is termed limiting droplet number ( $N_d^{lim}$ ), following Kacarab et al.  
 739 (2020), and is essentially the maximum  $N_d$  that can be formed under these vertical velocity  
 740 conditions. The vertical-velocity regime is therefore strictly defined, whenever  $S_{max}$  drops  
 741 below  $0.1\%$  and  $N_d$  approaches  $N_d^{lim}$ . Conversely, when  $S_{max}$  in clouds exceeds  $0.1\%$ , droplet  
 742 formation in the BL of both measurement sites is in the aerosol-limited regime, as the  $S_{max}$  is  
 743 high enough for clouds to be responsive to aerosol changes.

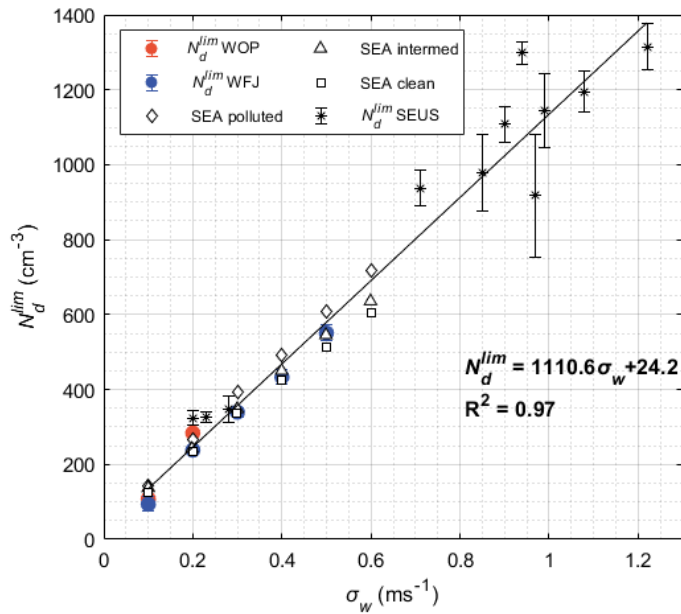
744 An alternative way of examining the  $N_d^{lim}$  response to changes in ~~the dispersion of~~  
 745 ~~updraft velocity  $\sigma_w$~~  is shown in Figure 9. ~~The limiting droplet number is defined within the~~  
 746 ~~vertical velocity regime, assuming that this regime prevails when  $S_{max}$  drops below  $0.1\%$ . It~~  
 747 ~~should be noted that the  $N_d^{lim}$  values shown on this figure are determined by calculating the~~  
 748 ~~averaged  $N_d$  achieved whenever  $S_{max} < 0.1\%$  for each examined  $\sigma_w$  value.~~ At WOP, droplet  
 749 formation is in the velocity-limited regime only for low  $\sigma_w$  values, namely  $0.1$  and  $0.2 \text{ ms}^{-1}$ ,  
 750 when the activated particles have more time to deplete the gas phase, and the  $S_{max}$  ~~that is~~ reached

Formatted: Font color: Auto



751 is that required to activate only the largest particles. At WFJ the prevailing dynamics create  
752 velocity-limited conditions even for more ~~convective~~turbulent boundary layers when  $\sigma_w$   
753 reaches up to  $0.5 \text{ ms}^{-1}$ .  $N_d^{lim}$  ( $\text{cm}^{-3}$ ) is linearly correlated with  $\sigma_w$  ( $\text{ms}^{-1}$ ) which can be described  
754 as  $N_d^{lim} = 1110.61137.9 \sigma_w + 24.2 - 17.1$  (Fig. 9). As a result, doubling  $\sigma_w$  from 0.1 to 0.2  
755  $\text{ms}^{-1}$  increases  $N_d^{lim}$  by  $\sim 60\%$  for both sites, while transitioning from 0.2 to  $0.4 \text{ ms}^{-1}$  further  
756 increases  $N_d^{lim}$  by  $\sim 45\%$ , and finally an additional  $\sim 20\%$  increase in  $N_d^{lim}$  occurs for WFJ  
757 for the  $0.4\text{-}0.5 \text{ ms}^{-1}$  velocity range. Remarkable agreement is seen for corresponding trends  
758 between  $N_d^{lim}$  and  $\sigma_w$  calculated for marine Stratocumulus clouds formed under extensive BB  
759 aerosol plumes over the Southeast Atlantic (SEA) Ocean (Kacarab et al., 2020), along with BL  
760 clouds formed in the Southeast United States (SEUS) (~~Bougiatioti et al., 2020~~)(Bougiatioti et  
761 al., 2020). Both studies have followed the same probabilistic approach for computing  $N_d$  as the  
762 one followed here. This realization is important as it implies that for regions where velocity-  
763 limited conditions are expected (i.e. under particularly high particle loads),  $N_d \sim N_d^{lim} \sim N_d^{lim}$   
764 and the  $N_d^{lim}$ - $\sigma_w$  relationship can be used to diagnose  $\sigma_w$  from retrievals of droplet number for  
765 virtually any type of BL cloud ~~-, using a number of established methods (e.g. Snider et al.,~~  
766 2017; Grosvenor et al., 2018).

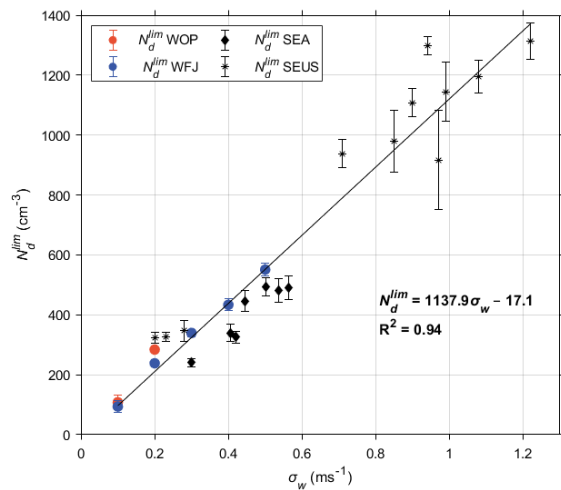
Formatted: Not Highlight



767  
 768 **Figure 9.** Limiting droplet number ( $\text{cm}^{-3}$ ) against the standard deviation of updraft velocity  
 769 ( $\text{ms}^{-1}$ ), calculated when vertical velocity conditions are met over WOP (orange trace) and WFJ  
 770 (blue trace) sites throughout the period of interest. Superimposed are the corresponding values  
 771 calculated for polluted (rhombuses), intermediate (triangles) and clean (squares) conditions  
 772 over the SEA Ocean and over the SEUS (asterisks).

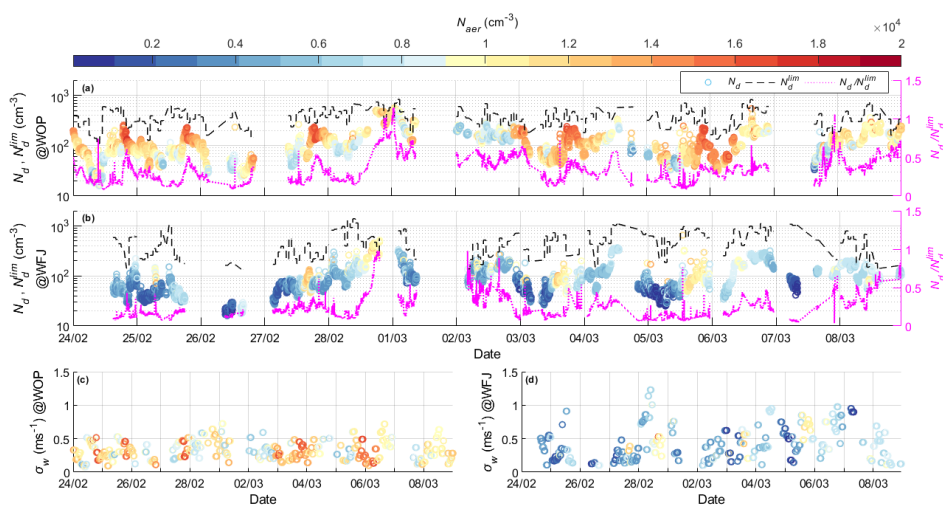
773  
 774 3.2.4  $\sigma_w$  and observed  $N_d$  determine if droplet formation is aerosol- or velocity-limited

775 Observations of  $N_d$  when compared against  $N_d^{lim}$  can potentially be used to deduce if droplet  
 776 formation is velocity- or aerosol-limited. This is important because it indicates whether aerosol  
 777 fluctuations are expected to result in substantial droplet number  $N_d$  responses in clouds. The  
 778 strong correlation between  $\sigma_w$  and  $N_d^{lim}$  enables this comparison. From the  $\sigma_w$  timeseries  
 779 together with the linear  $N_d^{lim}$ - $\sigma_w$  relationship (Section 3.2.3; Fig. 9) we obtain estimates of  $N_d^{lim}$   
 780 for both measurement stations (black dashed line in Fig. 10a, b) and the ratio  $N_d/N_d^{lim}$   
 781 (magenta dotted lines in Fig. 10a, b). The  $N_d$  timeseries calculated for WOP tend to be  
 782 approximately one third of  $N_d^{lim}$  for most of the observational period (colored circles in Fig.  
 783 10a, b), while for WFJ the same ratio is even lower  $\sim 1/4$ . Focusing on the relatively short  
 784 periods when  $S_{max}$  values drop below 0.1%, we estimate that droplet formation over both  
 785 measurement sites enters a velocity-limited regime when the ratio  $N_d/N_d^{lim}$  exceeds a critical  
 786 value of 0.565, with the most prevalent value being at  $\sim 0.79$  (supplement Fig. S4S6).



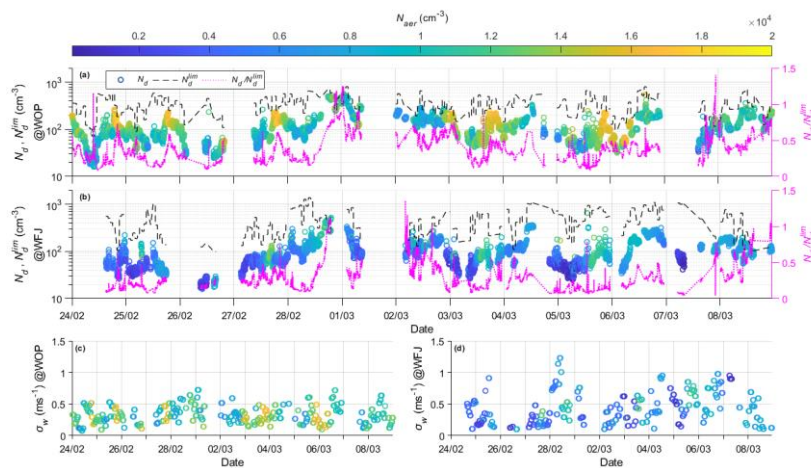
787

788 **Figure 9**



789

790 Limiting droplet number ( $\text{cm}^{-3}$ ) against the standard deviation of updraft velocities ( $\text{ms}^{-1}$ ),  
 791 calculated when vertical-velocity conditions are met over WOP (orange circles) and WFJ (blue  
 792 circles) sites throughout the period of interest. Superimposed are the corresponding values  
 793 calculated for clouds forming over the SEA Ocean (rhombuses) and over the SEUS (asterisks).



794  
 795 **Figure 10.** Timeseries of potential  $N_d$  ( $\text{cm}^{-3}$ ) (circles colored by **total aerosol number**  $N_{aer}$ ) along  
 796 with  $N_d^{lim}$  ( $\text{cm}^{-3}$ ) (black dashed line) and the ratio between those two (i.e.  $N_d/N_d^{lim}$ ) (magenta  
 797 dotted line), together with the timeseries of the calculated standard deviation of updraft  
 798 velocities ( $\text{ms}^{-1}$ ) (**circles colored by  $N_{aer}$** ), as estimated for WOP (a, c) and WFJ (b, d).

799  
 800 Throughout the period of interest velocity-limited conditions are met at WOP (WFJ)  
 801 with a frequency of  $\sim 0.5\%$  ( $\sim 2.5\%$ ) of the total time, reflecting again the sensitivity of droplet  
 802 formation to aerosol fluctuations. During nighttime however, when lower  $\sigma_w$  values ( $\sim 0.1 \text{ ms}^{-1}$ )  
 803 are recorded at WOP (Fig. 10c), we can observe some short periods characterized by  
 804 intermediate to high **aerosol levels**  $N_{aer}$  ( $> 1000 \text{ cm}^{-3}$ ) when the ratio  $N_d/N_d^{lim}$  exceeds  $\sim 0.565$ ,  
 805 indicating that droplet variability is driven by updraft velocity. ~~The standard deviation of~~  
 806 ~~updraft velocities~~ **The  $\sigma_w$  values** calculated at WFJ do not display a clear temporal pattern (Fig.  
 807 10d) but are generally higher than those recorded at the valley site. This is expected considering  
 808 the steepness of the topography than can cause updraft velocities to be higher, especially for  
 809 air-masses approaching the site from the north-easterly directions. Over the high mountain-top  
 810 site cloud formation is in the velocity-limited regime (i.e.  $N_d/N_d^{lim} \geq 0.565$ ) under high  
 811 ~~aerosol concentrations~~  $N_{aer}$  ( $\sim 1500 \text{ cm}^{-3}$ ) and higher  $\sigma_w$  conditions ( $\sim 0.8 \text{ ms}^{-1}$ ). These  
 812 conditions can be created when polluted air-masses from the valley site are vertically  
 813 transported to WFJ.

814

#### 4. Summary & ~~Conclusions~~ and conclusions

The current study focuses on the aerosol-CCN-cloud droplet interplay in Alpine clouds sampled during the RACLETS field campaign over a two-week period of measurements conducted in the valley (WOP), and at the mountain-top station (WFJ). Our main objective was to investigate the drivers of droplet formation in ~~mixed-phase clouds (MPCs)~~ formed in the region and understand in which situations ~~droplet number~~  $N_d$  is sensitive to aerosol perturbations.

Overall, lower  $N_{aer}$  ~~were~~ was systematically recorded at WFJ, indicating that the site is influenced by FT conditions. Deviations from this behavior are observed during fair weather conditions, when injections from the BL of lower altitudes can cause up to an order of magnitude elevation in the ~~aerosol concentrations~~  $N_{aer}$  measured at WFJ. Combining the particle size distribution and CCN number concentration measured at WFJ, the average hygroscopicity parameter  $\kappa$  is about 0.25, consistent with expectations for continental aerosol. The size-dependent  $\kappa$  reveals that accumulation mode particles are more hygroscopic than the smaller ones, which we attribute to an enrichment in organic material associated with primary emissions in the valley. The hygroscopicity of the particles at WFJ exhibit variations until February 28, which could reflect BL injections from the valley. Precipitation events occurring ~~during the second sub-period of interest~~ between 1 and 8 March, efficiently ~~remove particles~~ decrease  $N_{aer}$ , sometimes leaving some less hygroscopic particles.

Wind lidar products collected at WOP constrain the PDF of updraft ~~velocity~~ velocities, which combined with observed size distributions and hygroscopicity can be used to calculate the  $N_d$  in clouds. We show predictions to agree within 25% with the limited observations of ~~droplet number~~  $N_d$  available. While this degree of closure has been achieved in past studies for liquid-phase clouds, it has not been done at temperatures below freezing and with clouds containing ice – as done here.

~~When  $\sigma_w$  is equal to  $0.1 \text{ ms}^{-1}$  droplet formation over both measurement sites is always~~ Combining the potential  $N_d$  and the corresponding  $S_{max}$  with the aerosol-limited if size distribution data we sought to identify regimes where clouds formed are ~~aerosol concentrations~~ fall below  $\sim 300 \text{ cm}^{-3}$ . For intermediate and higher  $\sigma_w$  conditions ( $>0.3 \text{ ms}^{-1}$ ) the same behavior is seen, but the aerosol-limited regime is extended to higher aerosol concentrations  $\sim 10^3 \text{ cm}^{-3}$ . ~~When droplet formation is within the – or velocity-limited regime, it does not exceed a characteristic value,  $N_d^{lim}$ , that depends on  $\sigma_w$ .~~ We found that  $N_d^{lim}$  is reached, when sufficient ~~aerosol is present to decrease  $S_{max}$  below 0.1%,~~ Alpine clouds become velocity-limited, with

Formatted: Font color: Auto

Formatted: Font color: Auto

Formatted: Font color: Auto

Formatted: Font color: Auto

Formatted: Font color: Auto

848 ~~the  $N_d$  reaching an upper limit,  $N_d^{lim}$ , that depends on  $\sigma_w$  and corresponds to Velocity-limited~~  
849 ~~conditions occur~~ when  $N_d/N_d^{lim}$  is above 0.5 for both measurement sites (with a most likely  
850 ~~transition value at 0.7).~~65. Based on this understanding, we deduce that droplet formation  
851 throughout the period of interest appears most of the time to be aerosol-limited. More  
852 specifically, at the valley site, WOP, clouds become sensitive to updraft velocity variations  
853 only during nighttime, when the BL turbulence is low. Conversely, velocity-limited conditions  
854 are encountered at WFJ, during periods characterized by elevated aerosol and CCN  
855 concentration levels ( $>10^3 \text{ cm}^{-3}$ ) and higher  $\sigma_w$  values ( $\sim 0.8 \text{ ms}^{-1}$ ). Although variations in  
856 vertical velocity have not always been found to be the strongest factor influencing the cloud  
857 microphysical characteristics, correct consideration of updraft velocity fluctuations is crucial  
858 to fully understand the drivers of droplet variability and the role of aerosol as a driver of  $N_d$   
859 variability.

Formatted: Font color: Text 1

860 Interestingly, we find that the same linear relationship between  $N_d^{lim}$  and  $\sigma_w$  that  
861 describes the droplet formation during RACLETS holds for warm boundary layer clouds  
862 formed in the SE US (Bougiatioti et al., 2020) and in the SE Atlantic (Kacarab et al., 2019).  
863 This implies that the  $N_d^{lim}$ - $\sigma_w$  relationship may be universal, given the wide range of cloud  
864 formation conditions it represents. If so, measurements (or remote sensing) of ~~droplet~~  
865 ~~number  $N_d$~~  and vertical velocity distribution alone may be used to determine if cloud droplet  
866 formation is susceptible to aerosol variations or solely driven by vertical velocity – without any  
867 additional aerosol information.

Formatted: Font color: Auto

868 Approaching velocity-limited conditions also carries important implications for ice-  
869 formation processes in MPCs – as high ~~droplet number  $N_d$~~  means that droplet size and the  
870 probability of riming becomes minimum. Indeed, Lance et al. (2011) saw that the concentration  
871 of large droplets exceeding ~~30  $\mu\text{m}$~~ 30  $\mu\text{m}$  diameter – critical for rime splintering or droplet  
872 shattering to occur – drops considerably for polluted Arctic ~~mixed-phase clouds~~MPCs with  
873 ~~liquid content~~LWC  $\sim 0.2 \text{ g mgm}^{-3}$  and ~~droplet number  $N_d$~~   $\sim 300\text{-}400 \text{ cm}^{-3}$ . Assuming that these  
874 levels of ~~droplet number  $N_d$~~  reflects  $N_d^{lim}$ , the corresponding  $\sigma_w$  is  $0.3\text{-}0.35 \text{ ms}^{-1}$  (Fig. 9), which  
875 is characteristic for Arctic stratus. The same phenomenon can also occur in the Alpine clouds  
876 studied here, given that velocity-limited conditions ( $N_d/N_d^{lim} > 0.565$ ) occurs especially during  
877 nighttime (Fig. 10). Therefore, observations of ~~droplet number  $N_d$~~  and vertical velocity  
878 distribution (i.e.,  $N_d^{lim}$ ) may possibly be used to determine if SIP from riming and droplet  
879 shattering is impeded, and if occurring frequently enough may help explain the existence of  
880 persistent MPCs.

Formatted: Font color: Auto

881  
882 **Data Availability:** The data used in this study can be downloaded from the EnviDat data portal  
883 at <https://www.envidat.ch/group/about/raclets-field-campaign>. The meteorological  
884 measurements are provided by the Swiss Federal Office of Meteorology and Climatology  
885 MeteoSwiss at <https://gate.meteoswiss.ch/idaweb/login.do>. The Gaussian fits used for  
886 determining  $\sigma_w$  and the droplet parameterization used for the calculations in the study are  
887 available from [athanasios.nenes@epfl.ch](mailto:athanasios.nenes@epfl.ch) upon request.

888  
889 **Author Contributions:** PG and AN designed and initiated the study with methodology and  
890 software developed by AN. The analysis was carried out by PG and AN, with input from ABo,  
891 JW, CM, ZAK, JH, MH, ABe, UL. CCN instrumentation was setup by ABo, aerosol  
892 instrumentation and inlet setup ~~waswere~~ done by JW, CM and ZAK, cloud data by FR, JH,  
893 lidar data by MH. Instrument maintenance during the field campaign was carried out by JW  
894 and CM. Data curation was provided by PG, AN, JW, CM, FR. The original manuscript was  
895 written by PG and AN with input from all authors. All authors reviewed and commented on  
896 the manuscript.

897  
898 **Funding:** This study was supported by ~~Swiss Federal state funds~~, the European Research  
899 Council, CoG-2016 project PyroTRACH (726165) funded by H2020-EU.1.1. – Excellent  
900 Science, and from the European Union Horizon 2020 project FORCeS under grant agreement  
901 No 821205. JW, FR, ZAK, JH, UL acknowledge funding from the Swiss National Science  
902 Foundation (SNSF) grant number 200021\_175824. CM acknowledges funding from the SNSF  
903 grant number 200021\_169620.

904  
905 **Conflicts of Interest:** The authors declare no conflict of interest.

906 **References**

- 907 Andreae, M. O. and Rosenfeld, D.: Aerosol-cloud-precipitation interactions. Part 1. The nature  
908 and sources of cloud-active aerosols, *Earth-Science Rev.*, 89, 13–41,  
909 doi:10.1016/j.earscirev.2008.03.001, 2008.
- 910 [Baltensperger, U., Gäggeler, H. W., Jost, D. T., Lugauer, M., Schwikowski, M., Weingartner,  
911 E. and Seibert, P.: Aerosol climatology at the high-alpine site Jungfraujoch, Switzerland.  
912 \*J. Geophys. Res.\*, 102, 1997.](#)
- 913 Barahona, D., West, R. E. L., Stier, P., Romakkaniemi, S., Kokkola, H. and Nenes, A.:  
914 Comprehensively accounting for the effect of giant CCN in cloud activation  
915 parameterizations, *Atmos. Chem. Phys.*, 10, 2467–2473, doi:10.5194/acp-10-2467-2010,  
916 2010.
- 917 [Barahona, D., Molod, A., Bacmeister, J., Nenes, A., Gettelman, A., Morrison, H., Phillips, V.,  
918 and Eichmann, A.: Development of two-moment cloud microphysics for liquid and ice  
919 within the NASA Goddard Earth Observing System Model \(GEOS-5\). \*Geosci. Model  
920 Dev.\*, 7, 1733–1766, doi:10.5194/gmd-7-1733-2014, 2014.](#)
- 921 Beck, A., Henneberger, J., Schöpfer, S., Fugal, J. and Lohmann, U.: HoloGondel: In situ cloud  
922 observations on a cable car in the Swiss Alps using a holographic imager, *Atmos. Meas.  
923 Tech.*, 10, 459–476, doi:10.5194/amt-10-459-2017, 2017.
- 924 Bergeron, T.: On the physics of clouds and precipitation, Report, Int. Union Geod. Geophys.,  
925 doi:10.1038/174957a0, 1935.
- 926 Borys, R. D., Lowenthal, D. H., Cohn, S. A. and Brown, W. O. J.: Mountaintop and radar  
927 measurements of anthropogenic aerosol effects on snow growth and snowfall rate,  
928 *Geophys. Res. Lett.*, 30, doi:10.1029/2002gl016855, 2003.
- 929 Bougiatioti, A., Bezantakos, S., Stavroulas, I., Kalivitis, N., Kokkalis, P., Biskos, G.,  
930 Mihalopoulos, N., Papayannis, A. and Nenes, A.: Biomass-burning impact on CCN  
931 number, hygroscopicity and cloud formation during summertime in the eastern  
932 Mediterranean, *Atmos. Chem. Phys.*, 16, 7389–7409, doi:10.5194/acp-16-7389-2016,  
933 2016.
- 934 Bougiatioti, A., Nenes, A., Lin, J., Brock, C., de Gouw, J., Liao, J., Middlebrook, A. and Welti,  
935 A.: Drivers of cloud droplet number variability in the summertime Southeast United States,  
936 *Atmos. Chem. Phys. Discuss.*, 20, doi:10.5194/acp-20-12163-2020-225, ~~accepted for  
937 publication in ACP~~, 2020.
- 938 Chow, F. K., De Wekker, Stephan, F. J. and Snyder, B. J.: Mountain weather research and  
939 forecasting: recent progress and current challenges., Dordrecht: Springer, 2013. Internet



940 resource.

941 [Conant, W. C., VanReken, T. M., Rissman, T. A., Varutbangkul, V., Jonsson, H. H., Nenes,](#)  
942 [A., Jimenez, J. L., Delia, A. E., Bahreini, R., Roberts, G. C., Flagan, R. C., and Seinfeld,](#)  
943 [J. H.: Aerosol-cloud drop concentration closure in warm cumulus, \*J. Geophys. Res.-\*](#)  
944 [Atmos., 109, D13204, doi:10.1029/2003JD004324, 2004.](#)

945 Dusek, U., Frank, G. P., Curtius, J., Drewnick, F., Schneider, J., Krten, A., Rose, D., Andreae,  
946 M. O., Borrmann, S. and Pöschl, U.: Enhanced organic mass fraction and decreased  
947 hygroscopicity of cloud condensation nuclei (CCN) during new particle formation events,  
948 *Geophys. Res. Lett.*, 37, L03804, doi:10.1029/2009GL040930, 2010.

949 Fanourgakis, G. S., Kanakidou, M., Nenes, A., Bauer, S. E., Bergman, T., Carslaw, K. S., Grini,  
950 A., Hamilton, D. S., Johnson, J. S., Karydis, V. A., Kirkevåg, A., Kodros, J. K., Lohmann,  
951 U., Luo, G., Makkonen, R., Matsui, H., Neubauer, D., Pierce, J. R., Schmale, J., Stier, P.,  
952 Tsigaridis, K., van Noije, T., Wang, H., Watson-Parris, D., Westervelt, D. M., Yang, Y.,  
953 Yoshioka, M., Daskalakis, N., Decesari, S., Gysel Beer, M., Kalivitis, N., Liu, X.,  
954 Mahowald, N. M., Myriokefalitakis, S., Schrödner, R., Sfakianaki, M., Tsimpidi, A. P.,  
955 Wu, M. and Yu, F.: Evaluation of global simulations of aerosol particle number and cloud  
956 condensation nuclei, and implications for cloud droplet formation, *Atmos. Chem. Phys.*  
957 *Discuss.*, 19, 8591–8617, doi:10.5194/acp-19-8591-2019, 2019.

958 Farrington, R. J., Connolly, P. J., Lloyd, G., Bower, K. N., Flynn, M. J., Gallagher, M. W.,  
959 Field, P. R., Dearden, C. and Choularton, T. W.: Comparing model and measured ice  
960 crystal concentrations in orographic clouds during the INUPIAQ campaign, *Atmos. Chem.*  
961 *Phys.*, 16, 4945–4966, doi:10.5194/acp-16-4945-2016, 2016.

962 Field, P. R., Lawson, R. P., Brown, P. R. A., Lloyd, G., Westbrook, C., Moisseev, D.,  
963 Miltenberger, A., Nenes, A., Blyth, A., Choularton, T., Connolly, P., Buehl, J., Crosier, J.,  
964 Cui, Z., Dearden, C., DeMott, P., Flossmann, A., Heymsfield, A., Huang, Y., Kalesse, H.,  
965 Kanji, Z. A., Korolev, A., Kirchgaessner, A., Lasher-Trapp, S., Leisner, T., McFarquhar,  
966 G., Phillips, V., Stith, J. and Sullivan, S.: Chapter 7. Secondary Ice Production - current  
967 state of the science and recommendations for the future, *Meteorol. Monogr.*,  
968 doi:10.1175/amsmonographs-d-16-0014.1, 2017.

969 Findeisen, W.: Die kolloidmeteorologischen vorgänge bei der niederschlagsbildung, *Meteorol.*  
970 *Zeitschrift*, 55, 121–133, 1938.

971 Fountoukis, C. and Nenes, A.: Continued development of a cloud droplet formation  
972 parameterization for global climate models, *J. Geophys. Res.*, 110, D1121,  
973 doi:10.1029/2004JD005591, 2005.

974 Fountoukis, C., Nenes, A., Meskhidze, N., Bahreini, R., Conant, W. C., Jonsson, H., Murphy,  
975 S., Sorooshian, A., Varutbangkul, V., Brechtel, F., Flagan, R. C. and Seinfeld, J. H.:  
976 Aerosol-cloud drop concentration closure for clouds sampled during the International  
977 Consortium for Atmospheric Research on Transport and Transformation 2004 campaign,  
978 *J. Geophys. Res.*, 112, doi:10.1029/2006JD007272, 2007.

979 Fugal, J. P., Schulz, T. J. and Shaw, R. A.: Practical methods for automated reconstruction and  
980 characterization of particles in digital in-line holograms, *Meas. Sci. Technol.*, 20,  
981 doi:10.1088/0957-0233/20/7/075501, 2009.

982 Ghan, S., Guzman, G., and Abdul-Razzak, H.: Competition between sea salt and sulfate  
983 particles as cloud condensation nuclei, *J. Atmos. Sci.*, 55, 3340–3347, 1998.

984 Ghan, S.J., Abdul-Razzak, H., Nenes, A., Ming, Y., Liu, X., Ovchinnikov, M., Shipway, B.,  
985 Meskhidze, N., Xu, J., and Shi, X.: Droplet Nucleation: Physically-based  
986 Parameterization and Comparative Evaluation, *J. Adv. Model. Earth Syst.*, 3,  
987 doi:10.1029/2011MS000074, 2011.

988 Griesche, H. J., Seifert, P., Ansmann, A., Baars, H., Barrientos Velasco, C., Bühl, J.,  
989 Engelmann, R., Radenz, M. and Zhenping, Y.: Application of the shipborne remote  
990 sensing supersite OCEANET for profiling of Arctic aerosols and clouds during Polarstern  
991 cruise PS106, *Atmos. Meas. Tech. Discuss.*, (~~December~~), 1–37, doi:10.5194/amt-2019-  
992 434, 2019.

993 Grosvenor, D. P., Sourdeval, O., Zuidema, P., Ackerman, A., Alexandrov, M. D., Bennartz,  
994 R., Boers, R., Cairns, B., Chiu, J. C., Christensen, M., Deneke, H., Diamond, M., Feingold,  
995 G., Fridlind, A., Hünerbein, A., Knist, C., Kollias, P., Marshak, A., McCoy, D., Merk, D.,  
996 Painemal, D., Rausch, J., Rosenfeld, J., Russchenberg, H., Seifert, P., Sinclair, K., Stier,  
997 P., van Diedenhoven, B., Wendisch, M., Werner, F., Wood, R., Zhang, Z. and Quaas, J.:  
998 Remote sensing of droplet number concentration in warm clouds: A review of the current  
999 state of knowledge and perspectives. *Reviews of Geophysics*, 56, 409–453.  
1000 doi:10.1029/2017RG000593, 2018.

1001 Grubisic, V. and Billings, B. J.: Climatology of the Sierra Nevada mountain-wave events, *Mon.*  
1002 *Weather Rev.*, 136, 757–768, doi:10.1175/2007MWR1902.1, 2008.

1003 Hammer, E., Bukowiecki, N., Gysel, M., Jurányi, Z., Hoyle, C. R., Vogt, R., Baltensperger, U.  
1004 and Weingartner, E.: Investigation of the effective peak supersaturation for liquid-phase  
1005 clouds at the high-alpine site Jungfraujoch , Switzerland ( 3580 m a.s.l.), *Atmos.*  
1006 *Chem. Phys.*, 14, 1123–1139, doi:10.5194/acp-14-1123- 2014, 2014.

1007 Hammer, E., Bukowiecki, N., Luo, B. P., Lohmann, U., Marcolli, C., Weingartner, E.,

1008 Baltensperger, U. and Hoyle, C. R.: Sensitivity estimations for cloud droplet formation in  
1009 the vicinity of the high-alpine research station Jungfraujoch ( 3580 m a.s.l.), Atmos.  
1010 Chem. Phys., 15, 10309–10323, doi:10.5194/acp-15-10309-2015, 2015.

1011 Henneberg, O., Henneberger, J. and Lohmann, U.: Formation and development of orographic  
1012 mixed-phase clouds, J. Atmos. Sci., 74, 3703–3724, doi:10.1175/JAS-D-16-0348.1, 2017.

1013 Henneberger, J., Fugal, J. P., Stetzer, O. and Lohmann, U.: HOLIMO II: A digital holographic  
1014 instrument for ground-based in situ observations of microphysical properties of mixed-  
1015 phase clouds, Atmos. Meas. Tech., 6, 2975–2987, doi:10.5194/amt-6-2975-2013, 2013.

1016 Herrmann, E., Weingartner, E., Henne, S., Vuilleumier, L., Bukowiecki, N., Steinbacher, M.,  
1017 Conen, F., Collaud Coen, M., Hammer, E., Jurányi, Z., Baltensperger, U. and Gysel, M.:  
1018 Analysis of long-term aerosol size distribution data from Jungfraujoch with emphasis on  
1019 free tropospheric conditions, cloud influence, and air mass transport, J. Geophys. Res.  
1020 Atmos., 120, 9459–9480, doi:10.1002/2015JD023660, 2015.

1021 Hoyle, C. R., Webster, C. S., Rieder, H. E., Nenes, A., Hammer, E., Herrmann, E., Gysel, M.,  
1022 Bukowiecki, N., Weingartner, E., Steinbacher, M. and Baltensperger, U.: Chemical and  
1023 physical influences on aerosol activation in liquid clouds : a study based on observations  
1024 from the Jungfraujoch , Switzerland, Atmos. Chem. Phys., 16, 4043–4061,  
1025 doi:10.5194/acp-16-4043-2016, 2016.

1026 IPCC: Climate Change 2013: The Physical Science Basis. Contribution of Working Group I to  
1027 the Fifth Assessment Report of the Intergovernmental Panel on Climate Change, edited  
1028 by: Stocker, T. F., Qin, D., Plattner, G.-K., Tignor, M., Allen, S. K., Boschung, Cambridge  
1029 Univ. Press. Cambridge, UK New York, NY, USA, 1535 pp.,  
1030 doi:10.1017/CBO9781107415324, 2013.

1031 [Jensen, J. B. and Charlson R. J.: On the efficiency of nucleation scavenging, Tellus, 36B, 367–](#)  
1032 [375, doi: 10.3402/tellusb.v36i5.14917, 1984.](#)

1033 Jurányi, Z., Gysel, M., Weingartner, E., Decarlo, P. F., Kammermann, L. and Baltensperger,  
1034 U.: Measured and modelled cloud condensation nuclei number concentration at the high  
1035 alpine site Jungfraujoch, Atmos. Chem. Phys., 10, 7891–7906, doi:10.5194/acp-10-7891-  
1036 2010, 2010.

1037 Jurányi, Z., Gysel, M., Weingartner, E., Bukowiecki, N., Kammermann, L. and Baltensperger,  
1038 U.: A 17 month climatology of the cloud condensation nuclei number concentration at the  
1039 high alpine site Jungfraujoch, J. Geophys. Res., 116, D1020, doi:10.1029/2010JD015199,  
1040 2011.

1041 Kacarab, M., Lee Thornhill, K., Dobracki, A., Howell, S. G., O’Brien, J. R., Freitag, S., Poellot,

1042 M. R., Wood, R., Zuidema, P., Redemann, J. and Nenes, A.: Biomass burning aerosol as  
1043 a modulator of the droplet number in the southeast Atlantic region, *Atmos. Chem. Phys.*,  
1044 20, 3029–3040, doi:10.5194/acp-20-3029-2020, 2020.

1045 Kalkavouras, P., Bougiatioti, A., Kalivitis, N., Stavroulas, I., Tombrou, M., Nenes, A. and  
1046 Mihalopoulos, N.: Regional new particle formation as modulators of cloud condensation  
1047 nuclei and cloud droplet number in the eastern Mediterranean, *Atmos. Chem. Phys.*, 19,  
1048 6185–6203, doi:10.5194/acp-19-6185-2019, 2019.

1049 [Kammermann, L., Gysel, M., Weingartner, E. and Baltensperger, U.: 13-month climatology of](#)  
1050 [the aerosol hygroscopicity at the free tropospheric site Jungfraujoch \(3580 m a.s.l.\)](#),  
1051 [Atmos. Chem. Phys., 10, doi:10.5194/acp-10-10717-2010, 2010.](#)

1052 Kleissl, J., Honrath, R. E., Dziobak, M. P., Tanner, D., Val Martín, M., Owen, R. C. and  
1053 Helmig, D.: Occurrence of upslope flows at the Pico mountaintop observatory: A case  
1054 study of orographic flows on a small, volcanic island, *J. Geophys. Res. Atmos.*, 112,  
1055 D10S3, doi:10.1029/2006JD007565, 2007.

1056 Korolev, A. and Isaac, G.: Phase transformation of mixed-phase clouds, *Q. J. R. Meteorol.*  
1057 *Soc.*, 129, 19–38, doi:10.1256/qj.01.203, 2003.

1058 Lance, S., Shupe, M. D., Feingold, G., Brock, C. A., Cozic, J., Holloway, J. S., Moore, R. H.,  
1059 Nenes, A., Schwarz, J. P., Spackman, J. R., Froyd, K. D., Murphy, D. M., Brioude, J.,  
1060 Cooper, O. R., Stohl, A. and Burkhardt, J. F.: Cloud condensation nuclei as a modulator of  
1061 ice processes in Arctic mixed-phase clouds, *Atmos. Chem. Phys.*, 11, 8003–8015,  
1062 doi:10.5194/acp-11-8003-2011, 2011.

1063 Lanz, V. A., Přeřvot, A. S. H., Alfarra, M. R., Weimer, S., Mohr, C., Decarlo, P. F., Gianini, M.  
1064 F. D., Hueglin, C., Schneider, J., Favez, O., D’Anna, B., George, C. and Baltensperger,  
1065 U.: Characterization of aerosol chemical composition with aerosol mass spectrometry in  
1066 Central Europe: An overview, *Atmos. Chem. Phys.*, 10, 10453–10471, doi:10.5194/acp-  
1067 10-10453-2010, 2010.

1068 Latham, T. L., Beyersdorf, A. J., Thornhill, K. L., Winstead, E. L., Cubison, M. J., Hecobian,  
1069 A., Jimenez, J. L., Weber, R. J., Anderson, B. E. and Nenes, A.: Analysis of CCN activity  
1070 of Arctic aerosol and Canadian biomass burning during summer 2008, *Atmos. Chem.*  
1071 *Phys.*, 13, 2735–2756, doi:10.5194/acp-13-2735-2013, 2013.

1072 Lauber, A., Henneberger, J., Mignani, C., Ramelli, F., Pasquier, J., Wieder, J. and Lohmann,  
1073 U.: Continuous secondary ice production initiated by updrafts through the melting layer in  
1074 mountainous regions, 2020, ~~submitted~~.

1075 Lloyd, G., Choularton, T. W., Bower, K. N., Gallagher, M. W., Connolly, P. J., Flynn, M.,

1076 Farrington, R., Crosier, J., Schlenzcek, O., Fugal, J. and Henneberger, J.: The origins of  
1077 ice crystals measured in mixed-phase clouds at the high-alpine site Jungfraujoch, *Atmos.*  
1078 *Chem. Phys.*, 15, 12953–12969, doi:10.5194/acp-15-12953-2015, 2015.

1079 Lohmann, U.: A glaciation indirect aerosol effect caused by soot aerosols, *Geophys. Res. Lett.*,  
1080 29(4), doi:10.1029/2001GL014357, 2002.

1081 ~~Lohmann, U.: [Anthropogenic Aerosol Influences on Mixed-Phase Clouds](#), *Curr. Clim. Chang.*  
1082 *Reports*, 3, 32–44, doi:10.1007/s40641-017-0059-9, 2017.~~

1083 ~~Lohmann, U.~~ and Feichter, J.: Global indirect aerosol effects: a review, *Atmos. Chem. Phys.*,  
1084 5, 715–737, doi:10.5194/acp-5-715-2005, 2005.

1085 Lohmann, U., Henneberger, J., Henneberg, O., Fugal, J. P., Bühl, J. and Kanji, Z. A.:  
1086 Persistence of orographic mixed-phase clouds, *Geophys. Res. Lett.*, 43, 10512–10519,  
1087 doi:10.1002/2016GL071036, 2016.

1088 ~~[Lohmann, U.: Anthropogenic Aerosol Influences on Mixed-Phase Clouds](#), *Curr. Clim. Chang.*  
1089 *Reports*, 3, 32–44, doi:10.1007/s40641-017-0059-9, 2017.~~

1090 Meskhidze, N., Nenes, A., Conant, W. C. and Seinfeld, J. H.: Evaluation of a new cloud droplet  
1091 activation parameterization with in situ data from CRYSTAL-FACE and CSTRIFE, *J.*  
1092 *Geophys. Res.*, 110, D1620, doi:10.1029/2004JD005703, 2005.

1093 ~~Mignani, C., [Creamean, J. M.](#), [Zimmermann, L.](#), [Alewell, C.](#), and [Conen, F.](#): [New type of](#)  
1094 [evidence for secondary ice formation at around –15 °C in mixed-phase clouds](#), *Atmos.*  
1095 *Chem. Phys.*, 19, 877–886, doi:10.5194/acp-19-877-2019, 2019.~~

1096 ~~[Mignani, C.](#), Wieder, J., Sprenger, M. A., Kanji, Z. A., Henneberger, J., Alewell, C. and Conen,  
1097 F.: Towards ~~parameterising~~ atmospheric concentrations of ice-nucleating  
1098 particles active at moderate supercooling, *Atmos. Chem. Phys. Discuss.*, 21, 657–664,  
1099 doi:10.5194/acp-2020-524, 202021-657-2021, 2021.~~

1100 Moore, R. H., Bahreini, R., Brock, C. A., Froyd, K. D., Cozic, J., Holloway, J. S., Middlebrook,  
1101 A. M., Murphy, D. M. and Nenes, A.: Hygroscopicity and composition of Alaskan Arctic  
1102 CCN during April 2008, *Atmos. Chem. Phys.*, 11, 11807–11825, doi:10.5194/acp-11-  
1103 11807-2011, ~~in review~~, 2011.

1104 Morales Betancourt, R. and Nenes, A.: Characteristic updrafts for computing distribution-  
1105 averaged cloud droplet number and stratocumulus cloud properties, *J. Geophys. Res.*, 115,  
1106 D1822, doi:10.1029/2009JD013233, 2010.

1107 ~~Morales Betancourt, R. and Nenes, A.: [Understanding the contributions of aerosol properties](#)  
1108 [and parameterization discrepancies to droplet number variability in a global climate model](#),  
1109 *Atmos. Chem. Phys.*, 14, 4809–4826, doi:10.5194/acp-14-4809-2014, 2014.~~

1110 ~~Morales Betancourt, R.~~, Nenes, A., Jonsson, H., Flagan, R. C. and Seinfeld, J. H.: Evaluation  
1111 of an entraining droplet activation parameterization using in situ cloud data, *J. Geophys.*  
1112 *Res.*, 116, D1520, doi:10.1029/2010JD015324, 2011.

1113 ~~Morales Betancourt, R., and Nenes, A.:~~ Aerosol Activation Parameterization: The population  
1114 splitting concept revisited, *Geosci.Mod.Dev.*, 7, 2345–2357, doi:10.5194/gmd-7-2345-  
1115 2014, 2014.

1116 ~~Mosimann, L., Weingartner, E. and Waldvogel A.:~~ An analysis of accreted drop sizes and mass  
1117 on rimed snow crystals., *J. Atmos. Sci.*, 51, 1548–1558, 1994.

1118 Muhlbauer, A. and Lohmann, U.: Sensitivity studies of aerosol-cloud interactions in mixed-  
1119 phase orographic precipitation, *J. Atmos. Sci.*, 66, 2517–2538,  
1120 doi:10.1175/2009JAS3001.1, 2009.

1121 ~~Nenes, A. and Seinfeld, J. H.:~~ Parameterization of cloud droplet formation in global climate  
1122 models, *J. Geophys. Res.*, 108, 4415, doi:10.1029/2002jd002911, 2003.

1123 ~~Nenes, A., Ghan, S., Abdul-Razzak, H., Chuang, P.Y., Seinfeld, J.H.:~~ Kinetic Limitations on  
1124 Cloud Droplet Formation and Impact on Cloud Albedo, *Tellus*, 53B, 133-149, 2001.

1125 ~~Nenes, A. and Seinfeld, J. H.:~~ Parameterization of cloud droplet formation in global climate  
1126 models, *J. Geophys. Res.*, 108, 4415, doi:10.1029/2002jd002911, 2003.

1127 Okamoto, S. and Tanimoto, H.: A review of atmospheric chemistry observations at mountain  
1128 sites, *Prog. Earth Planet. Sci.*, 3, 34, doi:10.1186/s40645-016-0109-2, 2016.

1129 Petters, M. D. and Kreidenweis, S. M.: A single parameter representation of hygroscopic  
1130 growth and cloud condensation nucleus activity, *Atmos. Chem. Phys.*, 7, 1961–1971,  
1131 doi:10.5194/acp-7-1961-2007, 2007.

1132 Pringle, K. J., Tost, H., Pozzer, A., Pöschl, U. and Lelieveld, J.: Global distribution of the  
1133 effective aerosol hygroscopicity parameter for CCN activation, *Atmos. Chem. Phys.*, 10,  
1134 5241–5255, doi:10.5194/acp-10-5241-2010, 2010.

1135 Pruppacher, H. R. and Klett, J. D.: *Microphysics of Clouds and Precipitation*, ~~Kluwer Acad.~~  
1136 ~~Norwell, Mass~~ 2nd ed., 1997.

1137 Ramelli, F., Beck, A., Henneberger, J. and Lohmann, U.: Using a holographic imager on a  
1138 tethered balloon system for microphysical observations of boundary layer clouds, *Atmos.*  
1139 *Meas. Tech.*, 13, 925–939, doi:10.5194/amt-13-925-2020, 2020a.

1140 Ramelli, F., Henneberger, J., David, R. O., Lauber, A., Pasquier, J. T., Wieder, J., Bühl, J.,  
1141 Seifert, P., Engelmann, R., Hervo, M. and Lohmann, U.: Influence of low-level blocking  
1142 and turbulence on the microphysics of a mixed-phase cloud in an inner-Alpine valley,  
1143 *Atmos. Chem. Phys. Discuss.*, doi:10.5194/acp-2020-774, in review, 2020b.

1144 Ramelli, F., Henneberger, J., David, R. O., Bühl, J., Radenz, M., Seifert, P., Wieder, J., Lauber,  
1145 A., Pasquier, J. T., Engelmann, R., Mignani, C., Hervo, M. and Lohmann, U.:  
1146 Microphysical investigation of the seeder and feeder region of an Alpine mixed-phase  
1147 cloud, submitted manuscript, 2020c.

1148 Reutter, P., Su, H., Trentmann, J., Simmel, M., Rose, D., Gunthe, S. S., Wernli, H., Andreae,  
1149 M. O. and Pöschl, U.: Aerosol- and updraft-limited regimes of cloud droplet formation:  
1150 Influence of particle number, size and hygroscopicity on the activation of cloud  
1151 condensation nuclei (CCN), *Atmos. Chem. Phys.*, 9, 7067–7080, doi:10.5194/acp-9-7067-  
1152 2009, 2009.

1153 Roberts, G. C. and Nenes, A.: A continuous-flow streamwise thermal-gradient CCN chamber  
1154 for atmospheric measurements, *Aerosol Sci. Technol.*, 39(3), 206–221,  
1155 doi:10.1080/027868290913988, 2005.

1156 Roe, G. H.: Orographic Precipitation, *Annu. Rev. Earth Planet. Sci.*, 33, 645–671,  
1157 doi:10.1146/annurev.earth.33.092203.122541, 2005.

1158 Rose, D., Gunthe, S. S., Mikhailov, E., Frank, G. P., Dusek, U., Andreae, M. O. and Pöschl,  
1159 U.: Calibration and measurement uncertainties of a continuous-flow cloud condensation  
1160 nuclei counter (DMT-CCNC): CCN activation of ammonium sulfate and sodium chloride  
1161 aerosol particles in theory and experiment, *Atmos. Chem. Phys.*, 8(5), 1153–1179,  
1162 doi:10.5194/acp-8-1153-2008, 2008.

1163 Rotunno, R. and Houze, R. A.: Lessons on orographic precipitation from the Mesoscale Alpine  
1164 Programme, *Q. J. R. Meteorol. Soc.*, 133, 811–830, doi:10.1002/qj.67, 2007.

1165 Saleeby, S. M., Cotton, W. R., Lowenthal, D. and Messina, J.: Aerosol impacts on the  
1166 microphysical growth processes of orographic snowfall, *J. Appl. Meteorol. Climatol.*, 52,  
1167 834–852, doi:10.1175/JAMC-D-12-0193.1, 2013.

1168 Seinfeld, J. H. and Pandis, S. N.: *Atmospheric Chemistry and Physics: From Air Pollution to*  
1169 *Climate Change*, 2nd Edn., John Wiley, edited by: Hoboken, ~~New York, N. J.~~, 2006.

1170 Seinfeld, J. H., Bretherton, C., Carslaw, K. S., Coe, H., DeMott, P. J., Dunlea, E. J., Feingold,  
1171 G., Ghan, S., Guenther, A. B., Kahn, R., Kraucunas, I., Kreidenweis, S. M., Molina, M. J.,  
1172 Nenes, A., Penner, J. E., Prather, K. A., Ramanathan, V., Ramaswamy, V., Rasch, P. J.,  
1173 Ravishankara, A. R., Rosenfeld, D., Stephens, G. and Wood, R.: Improving our  
1174 fundamental understanding of the role of aerosol-cloud interactions in the climate system,  
1175 *Proc. Natl. Acad. Sci. U. S. A.*, 113, 5781–5790, doi:10.1073/pnas.1514043113, 2016.

1176 Smith, R. B.: Progress on the theory of orographic precipitation, *Spec. Pap. Geol. Soc. Am.*,  
1177 398, 1–16, doi:10.1130/2006.2398(01), 2006.

1178 ~~Sotiropoulou, G., Vignon, E., Young, G., Morrison, H., O'Shea, S. J., Lachlan-Cope T., Berne,~~  
1179 ~~A. and Nenes, A.: Secondary ice production in Antarctic mixed phase clouds: an~~  
1180 ~~underappreciated process in atmospheric models, Atmos. Chem. Phys. Discuss.,~~  
1181 ~~doi:<https://doi.org/10.5194/acp-2020-328>, 2020a.~~  
1182 Snider, J. R., Leon, D. and Wang, Z.: Droplet concentration and spectral broadening in  
1183 Southeast Pacific stratocumulus clouds, J. Atmos. Sci., 74(3), 719–749. doi:10.1175/JAS-  
1184 D-16-0043.1, 2017.  
1185 Sotiropoulou, G., Sullivan, S., Savre, J., Lloyd, G., Lachlan-Cope, T., Ekman, A. M. L. and  
1186 Nenes, A.: The impact of secondary ice production on Arctic stratocumulus, Atmos. Chem.  
1187 Phys., 20, 1301–1316, doi:10.5194/acp-20-1301-2020, ~~2020b~~2020.  
1188 Sotiropoulou, G., Vignon, É., Young, G., Morrison, H., O'Shea, S. J., Lachlan-Cope, T., Berne,  
1189 A., and Nenes, A.: Secondary ice production in summer clouds over the Antarctic coast:  
1190 an underappreciated process in atmospheric models. Atmos. Chem. Phys., 21, 755–771,  
1191 <https://doi.org/10.5194/acp-21-755-2021>, 2021.  
1192 Sud, Y.C., Lee, D., Oreopoulos, L., Barahona, D., Nenes, A. and M.J. Suarez: Performance of  
1193 McRAS-AC in the GEOS-5 AGCM: aerosol-cloud-microphysics, precipitation, cloud  
1194 radiative effects, and circulation, Geosci. Model. Dev., 6, 57–79, doi:10.5194/gmd-6-57-  
1195 2013, 2013.  
1196 Sullivan, S. C., Lee, D., Oreopoulos, L. and Nenes, A.: Role of updraft velocity in temporal  
1197 variability of global cloud hydrometeor number, Proc. Natl. Acad. Sci. U. S. A., 113,  
1198 5791–5796, doi:10.1073/pnas.1514039113, 2016.  
1199 Sullivan, S. C., Barthlott, C., Crosier, J., Zhukov, I., Nenes, A. and Hoose, C.: The effect of  
1200 secondary ice production parameterization on the simulation of a cold frontal rainband,  
1201 Atmos. Chem. Phys., 18, 16461–16480, doi:10.5194/acp-18-16461-2018, 2018.  
1202 Tokay, A., Wolff, D. B. and Petersen, W. A.: Evaluation of the new version of the laser-optical  
1203 disdrometer, OTT parsivel, J. Atmos. Ocean. Technol., 31(6), 1276–1288,  
1204 doi:10.1175/JTECH-D-13-00174.1, 2014.  
1205 Touloupas, G., Lauber, A., Henneberger, J., Beck, A. and Lucchi, A.: A convolutional neural  
1206 network for classifying cloud particles recorded by imaging probes, Atmos. Meas. Tech.,  
1207 13(5), 2219–2239, doi:10.5194/amt-13-2219-2020, 2020.  
1208 Tröstl, J., Herrmann, E., Frege, C., Bianchi, F., Molteni, U., Bukowiecki, N., Hoyle, C. R.,  
1209 Steinbacher, M., Weingartner, E., Dommen, J., Gysel, M. and Baltensperger, U.:  
1210 Contribution of new particle formation to the total aerosol concentration at the high-  
1211 altitude site Jungfrauoch (3580masl, Switzerland), J. Geophys. Res. Atmos., 121, 11692–



- 1212 11711, doi:10.1002/2015JD024637, 2016.
- 1213 Twomey, S., Radiative properties of clouds, pp. 278 – 280, in Aerosol Effects on Climate, S.G.  
1214 Jennings Editor, The University of Arizona Press, Tucson, 1993.
- 1215 Vosper, S. B., Wells, H., Sinclair, J. A. and Sheridan, P. F.: A climatology of lee waves over  
1216 the UK derived from model forecasts, Meteorol. Appl., 20, 466–481,  
1217 doi:10.1002/met.1311, 2013.
- 1218 Wang, J., Lee, Y. N., Daum, P. H., Jayne, J. and Alexander, M. L.: Effects of aerosol organics  
1219 on cloud condensation nucleus (CCN) concentration and first indirect aerosol effect,  
1220 Atmos. Chem. Phys., 8, 6325–6339, doi:10.5194/acp-8-6325-2008, 2008.
- 1221 Wegener, A.: Thermodynamik der Atmosphäre, Ger. Barth, Leipzig, 331 pp., 1911.
- 1222 Zubler, E. M., Lohmann, U., Lüthi, D., Schär, C. and Muhlbauer, A.: Statistical analysis of  
1223 aerosol effects on simulated mixed-phase clouds and precipitation in the Alps, J. Atmos.  
1224 Sci., 68, 1474–1492, doi:10.1175/2011JAS3632.1, 2011.

1225

Formatted: Indent: Left: 0", First line: 0"